https://doi.org/10.5194/se-2020-89
Preprint. Discussion started: 27 May 2020

Solid Earth
Discussions
Open Access
EGU

Towards the application of Stokes flow equations to structural restoration simulations

Melchior Schuh-Senlis[1], Cedric Thieulot[2], Paul Cupillard[1], and Guillaume Caumon[1]

[1]Université de Lorraine, CNRS, GeoRessources, France- 54000 Nancy, France
[2]Utrecht University, Netherlands

Correspondence: Melchior Schuh-Senlis (melchior.schuh-senlis@univ-lorraine.fr)

Abstract.

Structural restoration is commonly used to assess the deformation of geological structures and to reconstruct past basin geometries. To replace geometric criteria, linear elastic behavior and frictionless fault contact assumptions used in existing restoration approaches, we study the possibility of using a creeping flow behavior in geomechanical restoration. Indeed, salt rock in particular has been shown to behave as a Stokes viscous fluid over geological time scales, and faults appear in rocks reaching a plastic limit inside a shear zone. We have therefore developed a new approach for restoration based on considering geologic materials as highly viscous quasi-static fluids. The Stokes equations are solved for the velocity inside a model at each time step using only the material properties of the objects inside the model, their geometry and the current state of boundary conditions. The restoration is then achieved by advecting the material in the opposite direction of the forward velocity. Several benchmarks are presented to validate the results of the simulation code used to test the approach. This method is applied on simple two-dimensional geological cross-sections in confined conditions and shows that reasonable restored geometries can be obtained.

1 Introduction

The Earth's subsurface is the result of millions of years of deformation. Determining the deformation history from present-day structures has been a concern for geoscientists who try to understand and quantify basin evolution. Restoration is an ensemble of methods which allow such quantification, by reversing processes that led to the current geometry of a geological region (e.g., Chamberlin, 1910; Dahlstrom, 1969). It covers a number of different processes and methodologies. The classical techniques are unfolding and unfaulting using length/area preservation in order to remove the effects of tectonic forces. In addition to this, several methods have been developed to take into account the effects of other important parameters, like erosion and deposition of sediments (e.g., Dimakis et al., 1998), isostasy compensation (e.g., Allen and Allen, 2013), thermal subsidence due to mantle thermal effect (Royden and Keen, 1980; Allen and Allen, 2013), rock decompaction due to a change of load (e.g., Athy, 1930; Durand-Riard et al., 2011; Allen and Allen, 2013), or, at a smaller scale, the reverse migration of channelized systems (e.g., Parquer et al., 2017). These methods allow us to evaluate the consistency of a model and test the hypotheses which lead to its construction, in order to generate paleo-basin geometries consistent with present-day observations for use in more elaborate

https://doi.org/10.5194/se-2020-89
Preprint. Discussion started: 27 May 2020

hydro-mechanical forward models (e.g., Bouziat et al., 2019). In this article, we focus on the structural restoration based on unfolding and unfaulting.

Since the beginning of the last century, unfolding and unfaulting has been mostly done with geometric and kinematic rules (e.g., Chamberlin, 1910; Dahlstrom, 1969; Gratier, 1988; Rouby, 1994; Groshong, 2006; Medwedeff et al., 2016; Fossen, 2016). The first implementations in two dimensions (2D) used balancing restoration, relying on the conservation of layer bed area and thickness (e.g., Chamberlin, 1910; Dahlstrom, 1969; Groshong, 2006). Map restoration was then developed to study deformations which are mainly horizontal; it can be qualified as a 2.5D method (e.g., Cobbold and Percevault, 1983; Rouby, 1994; Ramón et al., 2016). Later, three dimensional (3D) geometrical methods have been proposed (Massot, 2002; Muron, 2005; Medwedeff et al., 2016), allowing the tracking of internal volumetric deformation. Such methods are all based on the minimization of horizon deformation and on volume conservation, and therefore considerably simplify rock deformation mechanisms and ignore mechanical layering effects. In this light, numerous authors have stressed out the necessity of incorporating mechanics into the restoration of geological models (Fletcher and Pollard, 1999; Muron, 2005; Maerten and Maerten, 2006; Moretti, 2008; Guzofski et al., 2009; Al-Fahmi et al., 2016).

Volumetric mechanics-based restoration has been developed since the 2000s as a geomechanical simulation with specific boundary values (Maerten and Maerten, 2001; De Santi et al., 2002; Muron, 2005; Moretti et al., 2006; Maerten and Maerten, 2006; Guzofski et al., 2009; Durand-Riard et al., 2010, 2013a, b; Tang et al., 2016; Chauvin et al., 2018). In this approach, internal deformation is not known *a priori*, and the strain is computed from the mechanical behavior of rocks and the applied boundary conditions. The model is parameterized with elastic properties to mimic the response of rocks to mechanical stresses and the restoration displacement is computed by solving the equation of motion, in which the Cauchy stress tensor is defined by Hooke's law. The restoration itself is performed by applying specific boundary conditions to constrain the model. These conditions, usually imposed on the displacement, rely on the following assumptions: the uppermost horizon was flat and horizontal at deposition time, and it was not faulted. Other conditions can be introduced as complementary geological knowledge, such as direction and scale of deformation, or amount of lateral displacement (Chauvin et al., 2018).

Although these methods offer significant advances in the structural restoration of geological models, they still present many limitations. First, the boundary conditions set to unfold and unfault the medium are unphysical (Lovely et al., 2012; Chauvin et al., 2018). Moreover, these conditions are convenient hypotheses which do not necessarily reflect the paleo-stress state, hence they can be questionned (Durand-Riard et al., 2010; Lovely et al., 2012; Durand-Riard et al., 2013a). Secondly, geomechanical restoration so far only considers elastic rock properties, neglecting other possible behaviors, such as viscous, visco-elastic or plastic deformation (Gerbault et al., 1998). Transverse isotropic behavior also affects strain localization during restoration (Durand-Riard et al., 2013a), but such a behavior is rarely applied in practice. These physical issues raise the question of the capability of geomechanical restoration to properly recover paleo-deformation. As a consequence, there are no clear guidelines on which method to choose between geometric and kinematic restoration and geomechanical restoration, despite the more physical approach of the second one (Maerten and Maerten, 2006; Guzofski et al., 2009). Moreover, in spite of its name,

https://doi.org/10.5194/se-2020-89
Preprint. Discussion started: 27 May 2020


Solid Earth Discussions

geomechanical restoration is extensively controlled by geometric considerations: flattening of the top layer and a geometric unfaulting based on frictionless contact conditions to stitch the horizon cutoff lines accross each fault.

Another practical issue is the need for a valid volumetric mesh of the structural model, including a boundary representation of the geological domain with the horizons and faults as boundaries (e.g., Muron, 2005), even if the use of implicit horizons relaxes this constraint (Durand-Riard et al., 2010). Such a mesh is difficult to generate, as shown for example by Pellerin et al. (2014), Zehner et al. (2016) and Anquez et al. (2019). Since restoration deals with large deformations, the model evolves and may need to be remeshed, limiting the applicability of the geomechanical restoration to be used as an interpretation validation tool.

To sum up, geomechanical restoration has overcome some limitations of the "classical" geometric restoration process, by taking some of the internal movement of the layers into account for example, but it still needs to be improved to better account for different rheologies, larger deformations, faults, salt tectonics, and boundary conditions. In this paper, we investigate a new method to address these challenges: instead of doing forward mechanical simulations with elastic motion and specific boundary conditions, we consider the rocks as viscous fluids to compute the motion. This is motivated by three main factors. First, rocks can behave as viscous fluids when subjected to deformation that includes large stress and strain over periods of millions of years (Massimi et al., 2006; Cornet, 2015). This principle has been used for more than three decades to simulate the flow of lithospheric scale to deep mantle material (Poliakov et al., 1993; Fullsack, 1995; Hassani et al., 1997; Schubert et al., 2001; Morra and Regenauer-Lieb, 2006; Thieulot, 2011; Gerya, 2019; Robey and Puckett, 2019; Louis-Napoléon et al., 2020), so there is extensive litterature on how to solve the associated equations. Secondly, considering the rocks as having a creeping flow behavior allows the simulation to reproduce the flow of salt layers (Nalpas and Brun, 1993), and possibly also other rock rheologies through relevant effective viscosities (Moresi et al., 2003; Glerum et al., 2018). Finally, the (isothermal) Stokes equations, which are used to compute the deformation of creeping fluids, are reversible, so they can be used to compute the restoration motion of a model with more physical boundary conditions and a backward advection scheme.

The outline of this paper is as follows: we first present the concepts of a Stokes flow-based restoration scheme and its physical underpinnings. In a second part, we introduce the numerical code we developed for this application. Finally, we show the results that were obtained on an upscaled version of the model presented by van Keken et al. (1997), on a more complicated model with a layered overburden, and on a model with no prior knowledge on the material properties and boundary conditions to apply.

2 Using creeping flow equations for geomechanical restoration

2.1 Creeping flow equations

The standard equations for creeping flows are the Stokes equations, consisting of the momentum conservation equation

$$\nabla \cdot \boldsymbol{\sigma} + \boldsymbol{f} = \mathbf{0} \tag{1}$$

https://doi.org/10.5194/se-2020-89
Preprint. Discussion started: 27 May 2020

and the mass conservation equation for incompressible fluids (continuity equation)

$$\boldsymbol{\nabla} \cdot \boldsymbol{v} = 0, \tag{2}$$

where $\boldsymbol{\nabla}$ is the del operator, $\boldsymbol{\sigma}$ is the stress tensor, $\boldsymbol{f}$ is the specific body force (usually the volumetric weight $\rho \boldsymbol{g}$), and $\boldsymbol{v}$ is the velocity. This is justified by the fact that the materials we deal with here are highly viscous (with a viscosity η over 10^{17} Pa.s) and move at sufficiently low speed for the inertial part of their movement to be neglected (Massimi et al., 2006). The stress consists of a deviatoric part $\boldsymbol{\tau}$ and an isotropic pressure p:

$$\boldsymbol{\sigma} = \boldsymbol{\tau} - p\mathbf{I}, \tag{3}$$

where $\mathbf{I}$ is the identity tensor. In the viscous flow assumption, the deviatoric part of the stress is

$$\boldsymbol{\tau} = 2\eta\mathbf{D}, \tag{4}$$

with η the dynamic viscosity and $\mathbf{D}$ the infinitesimal strain rate tensor defined by

$$\mathbf{D} = \frac{1}{2}\left[\boldsymbol{\nabla}\boldsymbol{v} + (\boldsymbol{\nabla}\boldsymbol{v})^T\right]. \tag{5}$$

Assembling Eq. (1), (3), (4) and (5), the momentum conservation equation can be written

$$\boldsymbol{\nabla} \cdot \left[\eta(\boldsymbol{\nabla}\boldsymbol{v} + (\boldsymbol{\nabla}\boldsymbol{v})^T)\right] - \boldsymbol{\nabla} p = -\rho \boldsymbol{g}. \tag{6}$$

2.2 Restoration idea

In forward simulation schemes, the Stokes equations (6) and (2) are solved for pressure and velocity, and the material representation of the geological model is advected from the velocity at each time step. This can for example be done by an Euler scheme, the position $\boldsymbol{x}(t + \Delta t)$ of each point of the material model after one time step being computed as

$$\boldsymbol{x}(t + \Delta t) = \boldsymbol{x}(t) + \boldsymbol{v}(t) \cdot \Delta t, \tag{7}$$

with $\boldsymbol{x}(t)$ the position and $\boldsymbol{v}(t)$ the computed velocity of the point at time t, and Δt the time step. This Finite-Difference approximation relies on the idea that if the chosen time step Δt is small enough, we can approximate the velocity of a particle as a constant over this time step (Δt is usually calculated using a Courant-Friedrichs-Lewy (CFL) condition to ensure it). Since the Stokes equations are linear and do not depend on previous time steps for the computation of the velocity, we can extend this approximation to backwards simulations. This will be the basis for the proposed restoration scheme: instead of applying Eq.(7), we will apply

$$\boldsymbol{x}(t - \Delta t) = \boldsymbol{x}(t) - \boldsymbol{v}(t) \cdot \Delta t \tag{8}$$

for the advection of the points of the material model, at each time step, like in Fig. 1.

In this light, using viscous fluid properties instead of elastic properties to represent the mechanical behavior of geological materials holds several advantages, such as the use of boundary conditions that are closer to reality, like a free surface on top, or the account of other rheologies like a salt layer.

https://doi.org/10.5194/se-2020-89
Preprint. Discussion started: 27 May 2020

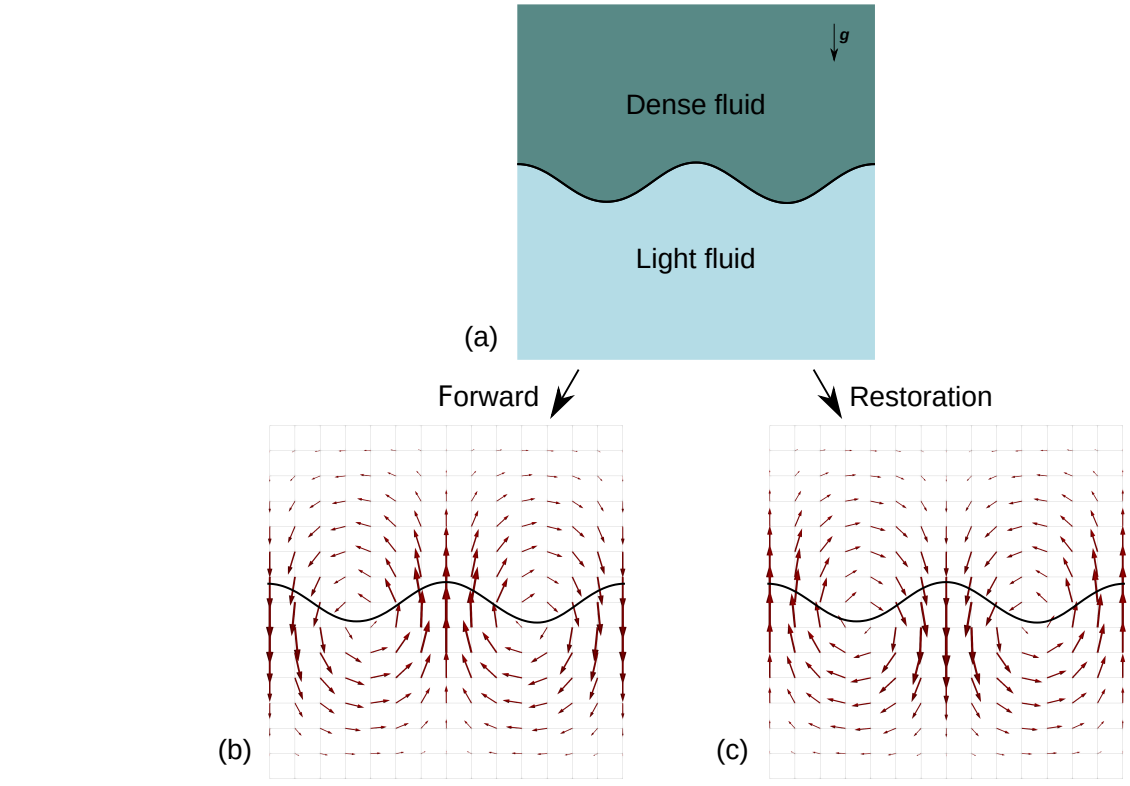

Figure 1. Example of the restoration scheme for a simple setup (a): as the arrows in (b) represent the velocity computed at a specific time step for a forward scheme, the advection of the material model in a restoration scheme is done with the opposite of the computed velocity, shown in (c).

3 Implementation in a specific code

3.1 Presentation

The restoration scheme presented in Sect. 2 has been implemented in the FAIStokes[1] code. It relies almost entirely on the deal.II library (Bangerth et al., 2007; Arndt et al., 2019, 2020) for all Finite Element related algorithms. The material tracking is based on the Particle-In-Cell (PIC) method (e.g., Asgari and Moresi, 2012; Thielmann et al., 2014; Gassmöller et al., 2016, 2018, 2019; Trim et al., 2019). The general workflow of the code is shown in Fig. 2 and details of implementation are discussed in the following sub-sections. Five benchmarks have been implemented to test the computation parts of the code and are presented in Appendices A, B, C, E and F. The possibility of a free surface on the top of the model has been implemented and benchmarked in forward simulations, but it has been proven to be unstable in backward simulations. Readers are refered to Appendix D for more details on this part, and to Sect. 5 for a discussion on the free surface backward instability.

[1] **F**inite element **A**rbitrary Eulerian-Lagrangian **I**mplementation of **Stokes**

https://doi.org/10.5194/se-2020-89
Preprint. Discussion started: 27 May 2020

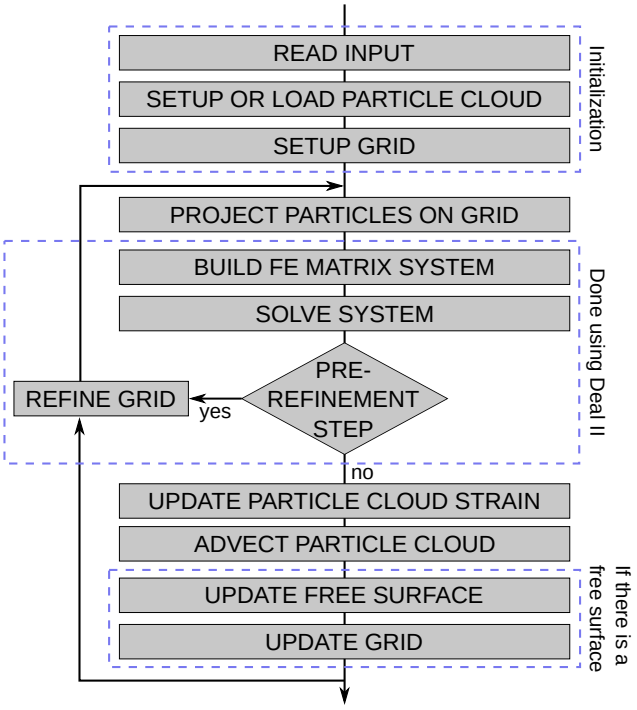

Figure 2. Schematic workflow of the FAIStokes code structure. The pre-refinement step occurs at the beginning of the simulation (or during a reinitialization of the grid) to ensure that the velocity used for the advection step is computed using the adaptively refined grid.

3.2 Finite Element discretization

The Finite Element Method (FEM) was introduced in the late 1950's (Hughes, 2012). Since then, it has emerged as one of the most powerful methods for solving Partial Differential Equations (PDEs) numerically. In FAIStokes, the FEM algorithms are based on the deal.II library. The domain is discretized on a set of quadrilateral elements, on which Finite Element (FE) basis functions are defined. The aim of this paper is not to do a thorough review of the FEM, so only the specifications of the FAIStokes code will be presented here. For solving the Stokes equations, we use quadrilateral Taylor-Hood $Q_2 \times Q_1$ elements that satisfy the Ladyzhenskaya-Babuška-Brezzi (LBB) condition for stability (Donea et al., 2004). Contrarily to many creeping flow codes that are used to study the subsurface, we do not solve the heat transport equation, both for simplicity and because it is likely to have only a small effect on the strain at the scale at which structural restoration is generally applied (i.e. basin-scale, close to the surface). We use Dirichlet and Neumann boundary conditions that we adapt (e.g. rigidity, free-slip, free surface, specific traction or velocity) for each boundary to the different problems at hand. Appendices A, B, E and F showcase results of the FE benchmarking.

https://doi.org/10.5194/se-2020-89
Preprint. Discussion started: 27 May 2020


Solid Earth
Discussions
Open Access
EGU

3.3 Material discretization

The geomechanical simulation of a specific domain requires to choose an appropriate kinematic description to follow the displacement inside the geological layers. Continuum mechanics first distinguished two main frames: the Eulerian frame of reference, also known as the spatial description, and the Lagrangian frame of reference, also known as the material description (Cornet, 2015). Both methods have their advantages and disadvantages, but neither of them is specifically adapted in the case of large displacements over time, such as those studied here. In order to overcome the limitations of the two approaches, the Arbitrary Lagrangian Eulerian (ALE) formulation (Fullsack, 1995; Donea et al., 2004), which inherits features from both methodologies, was developed. It has various formulations and implementations, both in 2D (e.g., Willett et al., 1993; Poliakov et al., 1996; Massimi et al., 2006, 2007; Fillon et al., 2013; Rose et al., 2017) and, more recently, in 3D (e.g., Braun, 2003; Ismail-Zadeh et al., 2004; Thieulot, 2011; Thieulot et al., 2014). Most of these methods rely on keeping track of the material properties in a Lagrangian way, while computing the displacement on a grid that can only deform vertically to account for an eventual free surface. It is particularly useful in geomechanics, where the vertical deformation is generally small compared to the horizontal deformation, and in the case of highly viscous fluids in the mantle, for which the density and viscosity depend mostly on the temperature and depth. In FAIStokes, the grid has an ALE part as it can adapt to follow the movement of the free surface.

3.4 The PIC method

During mechanical simulations, at each time step the material properties of the particles are projected onto the grid. They are then used to solve the Stokes equations on the grid. Following this, the particles are advected using the solution on the grid.

At the begining of the simulations, FAIStokes either creates a model from a function giving the distribution of the material parameters or loads a particle swarm from a file. In the first case, a regularly distributed particle swarm is generated, with a density of particles depending on the size of the smallest element of the computation grid. The given function is then used to associate the material properties to the particles depending on their position. Since the particle swarm doesn't directly track the interfaces, it has to be dense enough to recover accurately the material properties of the model; depending on the simulation, some parts of the model can therefore be densified to keep the appropriate accuracy. At each time step, the material properties are interpolated from the particle swarm to the grid in order to build the FE matrix and its preconditioner. For each element, the density is interpolated on the quadrature points using an arithmetic mean of the densities of the particles around the quadrature points (closer than a distance depending on the smallest element of the domain). The viscosity is recovered for each element using a harmonic mean of the viscosities of the particles inside the element. This reduces the effect of very high viscosity differences (possibly of several orders of magnitude) on the solver and is more computationally efficient despite the higher grid refinement needed (Deubelbeiss and Kaus, 2008; Thielmann et al., 2014; Heister et al., 2017). In the simulations we present hereafter, we were able to verify that this averaging verifies the conservation of the volume and mass in the model. Appendices A, B, E and F test the interpolation of the material properties from the particle swarm to the finite element grid to reasonable accuracy.

https://doi.org/10.5194/se-2020-89
Preprint. Discussion started: 27 May 2020

3.5 Grid and solvers

The grid and solvers come from the deal.II code, and their use is highly inspired from the deal.II tutorials $step-31$ [2] and $step-32$ [3]. The grid is created first as a quadrilateral from the coordinates of the bottom left and top right corners of the domain. This quadrilateral is then split in order to get cells closest to a square (depending on the model bounding box size) and refined and coarsened adaptively several times to construct the initial grid. The FE matrix, its preconditioner and the right-hand side force-vector are constructed using the material properties interpolated from the particle swarm as described in the previous subsection. In the right-hand side, the norm of the gravity vector $\boldsymbol{g}$ of Eq. (6) is always $9.81\ \mathrm{m.s}^{-2}$ in our simulations, and its direction is always downwards. The matrix system is then solved using an iterative FGMRES solver preconditioned by a block matrix involving the Schur complement (Kronbichler et al., 2012). This solution is then used to refine and coarsen the grid adaptively using deal.II's features, based on a gradient recovery estimator in order to minimize the local error. Depending on the input level of refinement, the cycle of building the matrix system, solving it, and adaptively refining and coarsening the grid is repeated several times, as shown in Fig. 2. Appendices A, B, E, F show the results of benchmarks that tested the computation of the velocity on different setups.

3.6 Velocity interpolation

Once the grid refinement has been completed, the particle swarm is advected by the obtained solution. In FAIStokes, the interpolation of the velocity is done separately in each grid cell with a Q_2 interpolation scheme. Depending on whether the simulation is forward or backward, the displacement of each particle for a time step Δt is computed using Eq. (7) or (8). The value of Δt is computed from the CFL condition. The default value for the CFL number is 0.085, but it can be reduced depending on the simulation (for example, the results shown in the next section use a CFL number of 0.0085, while the benchmarks in the Appendix use a CFL number of 0.042). The advection is done with a 2^{nd}-order Runge-Kutta scheme in space: at each time step, the particles are first advected by half the computed displacement; the velocity is then interpolated on their new position to update the displacement, and advect them again by half of this new displacement. This scheme reduces the error in the advection process without need for simulation time step refinements. It is computationally efficient because the computation of the displacement on the particle swarm is quite cheap compared to solving the FE matrix system. Appendices C, E, F show the results of benchmarks that tested the interpolation of the velocity in time-dependant problems.

4 Results

In addition to the benchmarks presented in the Appendices, which mainly check the algorithms of the code, we tested our specific restoration scheme on three simple models. In those experiments, the boundary conditions are simplified and quite unrealistic, but the goal here is to check the behavior of the reverse-time modeling in simple settings. In particular, we choose to neglect basal and lateral displacements which are known to play a role in salt tectonics (Koyi, 1996; Ismail-Zadeh et al.,

[2] https://dealii.org/9.0.0/doxygen/deal.II/step_31.html
[3] https://dealii.org/9.0.0/doxygen/deal.II/step_32.html

https://doi.org/10.5194/se-2020-89
Preprint. Discussion started: 27 May 2020

Solid Earth
Discussions
Open Access
EGU

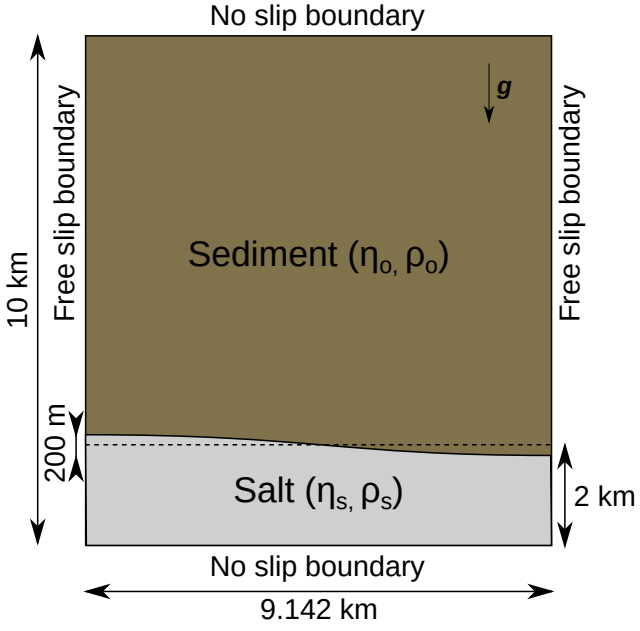

Figure 3. Setup of the model adapted from van Keken et al. (1997).

2004) but would require a calibration and would increase the degrees of freedom of the problem. Therefore, we choose to focus on tractable, density-driven physical models.

4.1 Diapiric growth model

The first model is scaled-up from van Keken et al. (1997). The setup consists of a simple two-layered system driven by gravity, as shown in Fig. 3. The upper layer represents sediments that are denser than the lower layer which contains salt ($\rho_o = 2600$ kg.m^{-3} for the sediment layer and $\rho_s = 2150$ kg.m^{-3} for the salt layer). A sinusoidal instability initiates the movement at the begining of the simulation. The model is limited to a 10 km $\times$ 9.142 km domain (the width value is given by van Keken et al. (1997) to yield the largest growth rate for the diapir) with free slip boundary conditions on the sides and no slip boundary conditions on the top and bottom sides. The grid has 32^2 initial elements and two levels of additional adaptive refinement. The particle swarm has a heterogeneous particle density: it is first sampled regularly in the model and then densified to five times more particles around the interface between the two layers to facilitate the tracking of material properties. The average distance between two particles near the interface is 14.3 m. The total number of particles is $64,000$. Two experiments were performed in this model: the first one as a test with isoviscous materials ($\eta_o = \eta_s = 10^{19}$ Pa.s), the second one with material properties closer to reality with a lower viscosity for salt ($\eta_o = 2.8 \times 10^{19}$ Pa.s for the sediment layer and $\eta_s = 1.4 \times 10^{17}$ Pa.s for the salt layer).

For each experiment, we first did a forward simulation, and then we applied the restoration scheme to the results obtained at the end of the simulation. The state obtained after 6×10^6 years for the first test and 1.5×10^6 years for the second test, as

https://doi.org/10.5194/se-2020-89
Preprint. Discussion started: 27 May 2020

Solid Earth
Discussions
Open Access
EGU

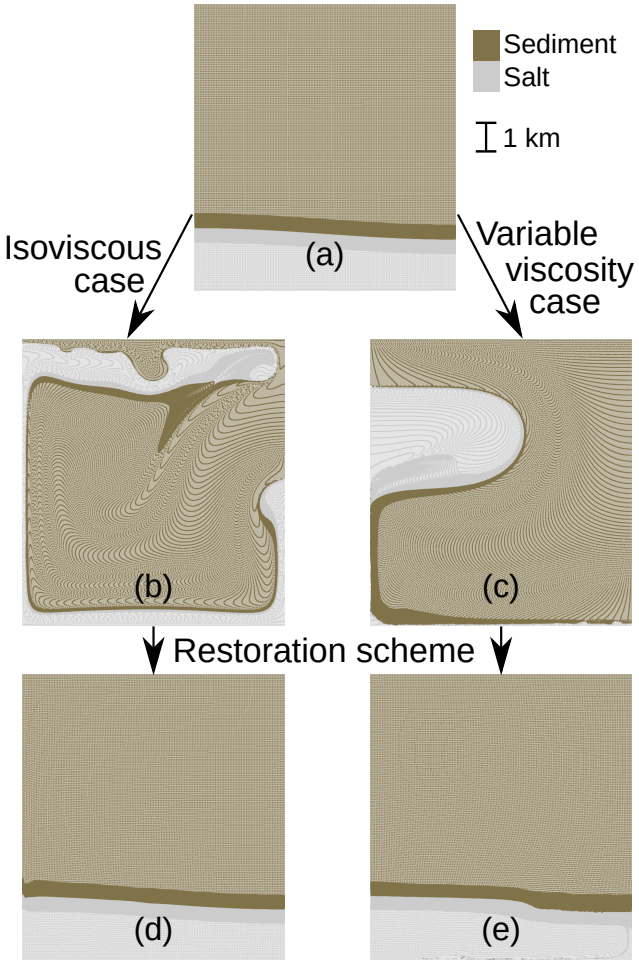

Figure 4. Particle swarms for the two synthetic diapiric growth experiments. The darker grey and brown parts on the swarms are due to the higher density of particles around the interfaces. The particles have the same initial position (a) in the two experiments, with different material properties. The result of the forward simulation after 6×10^6 years for the first experiment is shown in (b). (c) shows the result of the forward simulation for the second experiment after 1.5×10^6 years. The results for the restoration simulations are shown in (d) and (e) for the first and the second experiment, respectively.

well as the restored models, are shown in Fig. 4. We can see that while the isoviscous experiment has a rather smooth forward result, the second experiment with a less viscous salt leads to the creation of a salt weld (surface where the salt layer thickness has reached or almost reached zero, the salt having creeped away) at the bottom and left-hand side of the model.

In order to check the quality of the restoration in the two experiments, we compute for each particle the distance between its original position before the forward simulation and its position at the end of the restoration process. The mean value for this distance is 14 m (0.1% error) for the isoviscous case and 201 m (2% error) for the variable viscosity case, and the maximum value is 143 m (1.5% error) for the isoviscous case and 4947 m (49% error) for the variable viscosity case. While these results

https://doi.org/10.5194/se-2020-89
Preprint. Discussion started: 27 May 2020

Solid Earth
Discussions
Open Access
EGU

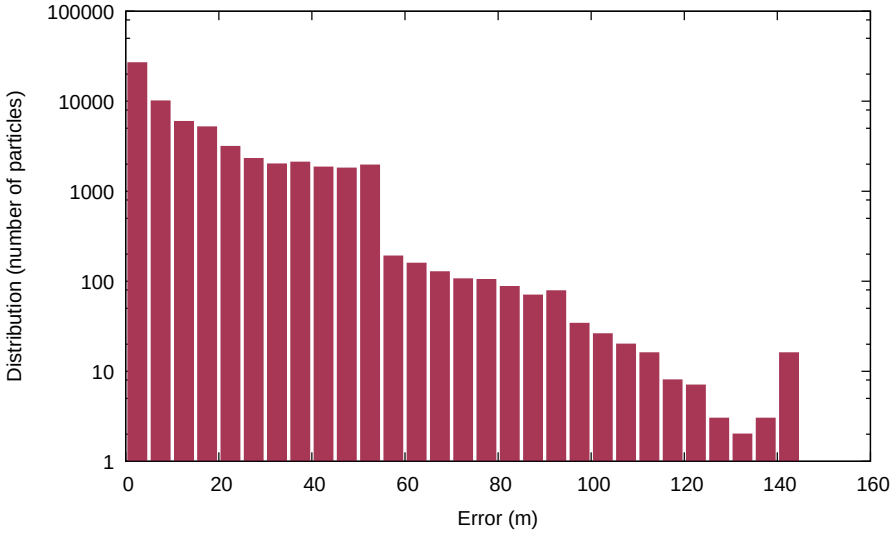

Figure 5. Error logarithmic distribution for the first experiment (isoviscosity) on the diapiric growth model.

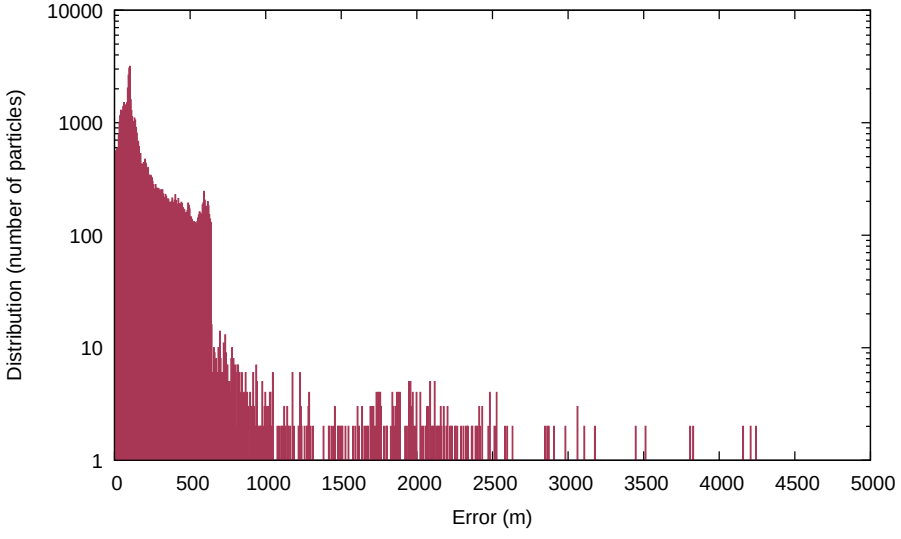

Figure 6. Error logarithmic distribution for the second experiment (variable viscosity) on the diapiric growth model.

are quite good for the isoviscous case, we could think that the variable viscosity case restoration is too inaccurate. Histograms for the errors in the two experiments are given in Fig. 5 and Fig. 6, and help explain this phenomenon. The high error values in the variable viscosity case are due to the creation of a basal weld, which mixes the particles at the bottom of the model. Some of these particles are not well restored and stay at the bottom of the model, creating very large errors (hence the error bars of 1 to 20 particles with an error higher than 500 m in Fig. 6). The basal weld in itself creates large distortions which explain the

https://doi.org/10.5194/se-2020-89
Preprint. Discussion started: 27 May 2020

overall large errors at the interface. However, if we look at the model at the end of the experiments with geologists eyes (i.e. in a global way, not taking into account small irregularities), and study only the boundary between the two layers, the maximum distance between the initial model and the restored model is only $50\ \mathrm{m}$ (0.5% error) for the first experiment and $125\ \mathrm{m}$ (1.25% error) for the second, which is acceptable considering the large amount of total deformation.

4.2 Layered overburden model

The domain size is $30\ \mathrm{km}$ horizontally and $10\ \mathrm{km}$ vertically. A salt layer is here enclosed between a basement layer and an overburden that consists of multiple layers. The top of the salt layer is slightly deformed to enable movement. The repartition of the material properties (ρ, η) in the layers is shown in Fig. 7. The values are relatively similar to those of the second experiment with the van Keken model, but the overburden has layers with slightly different material properties. Moreover, the top boundary condition is free slip, and the bottom of the salt layer is constrained by the basement layer. The side boundaries have a free slip condition. The grid has 16×48 initial elements and two levels of additional adaptive refinement. The particle swarm is composed of $307,200$ regularly distributed particles.

Like in the previous model, we first did a forward simulation spanning $350 \times 10^3\ \mathrm{years}$, and then we restored it. The results are shown in Fig. 7. We see that the restored model fits the initial state very well.

In the present setup, the movement of the salt layer depends on the folding and thinning of the sediment overburden. On both sides of the diapir, small basal welds are created. The distance between the initial position and restored position of the particles is computed, and its mean and maximum values are respectively $3\ \mathrm{m}$ and $639\ \mathrm{m}$. A close look at the restored model shows that the particles with a high error are actually very few (Fig. 8) and come from the welds (Fig. 9). If we look at the layer interfaces, the maximum distance between the initial and restored state is $90\ \mathrm{m}$, and is localized around the area of the welds (Fig. 10).

4.3 Stochastically generated salt diapir

This last model was generated with the method proposed by Clausolles et al. (2019). It consists of a salt diapir that mimicks passive diapirism structures created by syndeformation differential sediment loading. The shape of the salt diapir is generated by a stochastic method. The setup is quite simple but interesting for two reasons. First, this model was not created by a forward viscous simulation, and the rheology of the salt and sediments is not known. Second, this model has a high uncertainty and it is uncertain wether the boundary conditions we apply can restore it or not. Because of these two points, the restoration we perform here can be assimilated to the simplification of a real case application, in order to test the concept of the method with this type of geomodel. The initial particle swarm contains $102,510$ particles regularly sampling the model, and we apply free-slip boundary conditions on the top and side model boundaries, and a no slip boundary condition on the bottom. Figure 11 shows the initial state of the model. The grid has 48×80 initial elements and three levels of additional adaptive refinement; its state at the beginning of the simulation is shown in Fig. 12. In order to assess the influence of the value of the parameters on the results of the restoration, we tested different possibilities. For the density, the value for salt rock is $\rho_{salt} = 2160\ \mathrm{kg.m^{-3}}$, while the value for sediments can vary depending on the type and origin of deposition mechanisms; we considered here a value

https://doi.org/10.5194/se-2020-89
Preprint. Discussion started: 27 May 2020

Solid Earth
Discussions
Open Access
EGU

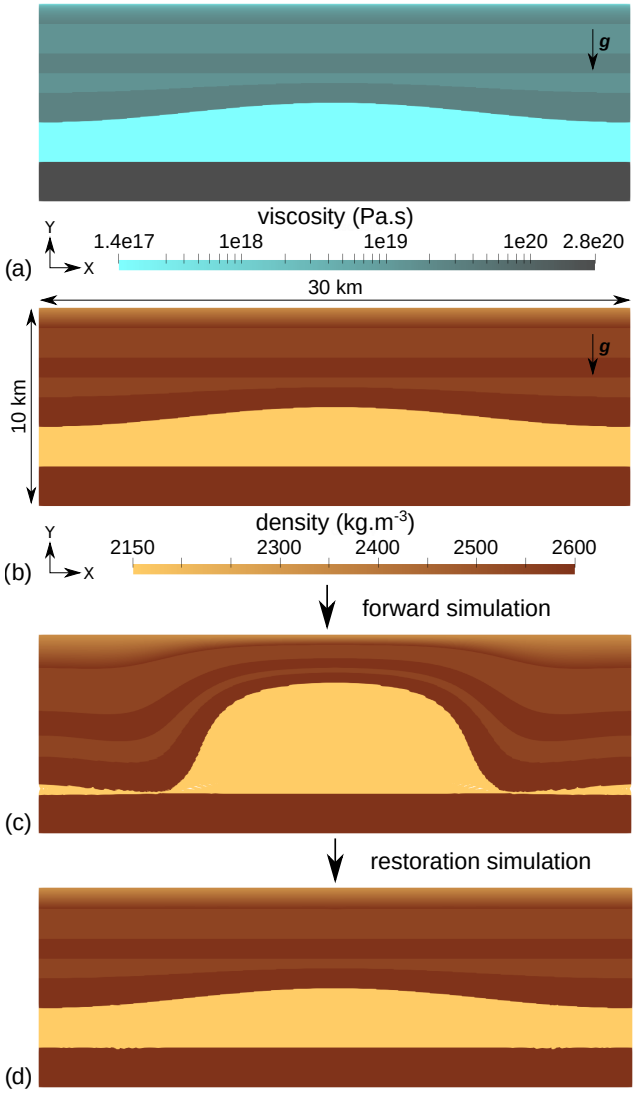

Figure 7. Setup and evolution of the layered overburden model. (a) and (b) show the material properties in the model, with the viscosity in logarithmic scale. The results of the simulations are shown at (a) the end of the forward simulation and (b) the end of the restoration simulation.

$\rho_o \in [2600; 3300]$ kg.m^{-3}. For simplicity, we set the viscosity of the salt layer at $\eta_{salt} = 10^{17}$ Pa.s and only vary the viscosity of the sediments $\eta_o \in \left[10^{19}; 10^{21}\right]$ Pa.s in order to test the effect of the constrast.

We did five experiments with different values of ρ_o and η_o:

- Exp.1: $\rho_o = 2600$ kg.m^{-3}, $\eta_o = 10^{19}$ Pa.s
- Exp.2: $\rho_o = 3300$ kg.m^{-3}, $\eta_o = 10^{19}$ Pa.s

https://doi.org/10.5194/se-2020-89
Preprint. Discussion started: 27 May 2020

Solid Earth
Discussions
Open Access
EGU

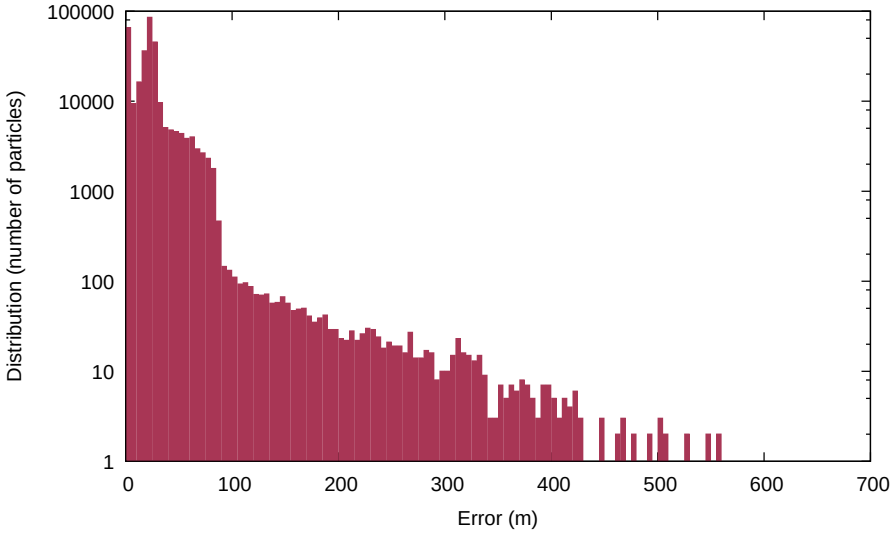

Figure 8. Logarithmic distribution of the error between the initial and restored model.

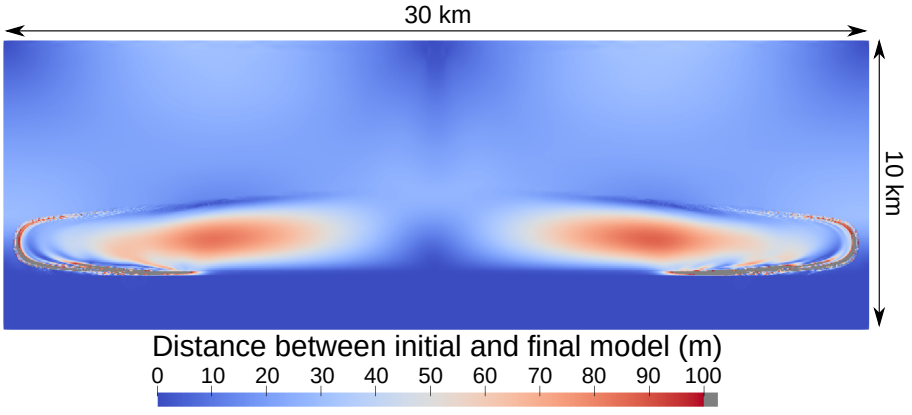

Figure 9. Distance between the initial and restored model. In grey, the points where the distance is higher than 100 m (1% error). We can see that those points are only located where the welds appear near the interfaces of the salt layer.

- Exp.3: $\rho_o = 2950$ kg.m^{-3}, $\eta_o = 10^{20}$ Pa.s
- Exp.4: $\rho_o = 2600$ kg.m^{-3}, $\eta_o = 10^{21}$ Pa.s
- Exp.5: $\rho_o = 3300$ kg.m^{-3}, $\eta_o = 10^{21}$ Pa.s

As this is a simplification of a real case application, and there is no information on the type of sediments, in each experiment the density and viscosity are homogeneous in the sediment and salt layers.

https://doi.org/10.5194/se-2020-89
Preprint. Discussion started: 27 May 2020

Solid Earth
Discussions
Open Access
EGU

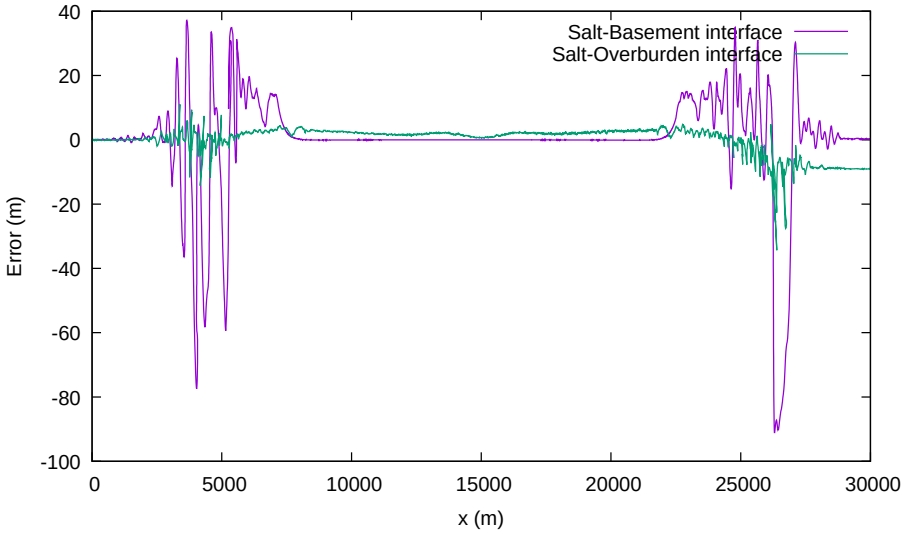

Figure 10. Difference between the initial and restored interfaces. The overall error is relatively small, the highest errors appears at the position of the welds for the interface between the salt layer and the basement layer (highest viscosity contrast).

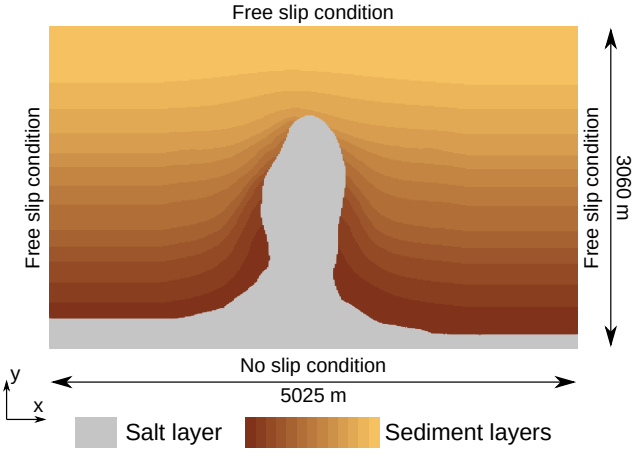

Figure 11. Setup of the simulation for the model generated with the method proposed by Clausolles et al. (2019). The initial model is sampled on a regularly spaced particle swarm.

The results for the 5 experiment simulations are given in Fig 13. Depending on the experiment, we choose to stop the restoration process after different durations t_{end}. Indeed, depending on the viscosity and density, the relaxation time is different for each experiment.

Overall, the restoration process removes the diapir and leaves a weld, while the sediment layers remain globally flat. Since this setup is generated by a method for syndeformation diapirs, a full restoration of the model should have taken into account

https://doi.org/10.5194/se-2020-89
Preprint. Discussion started: 27 May 2020

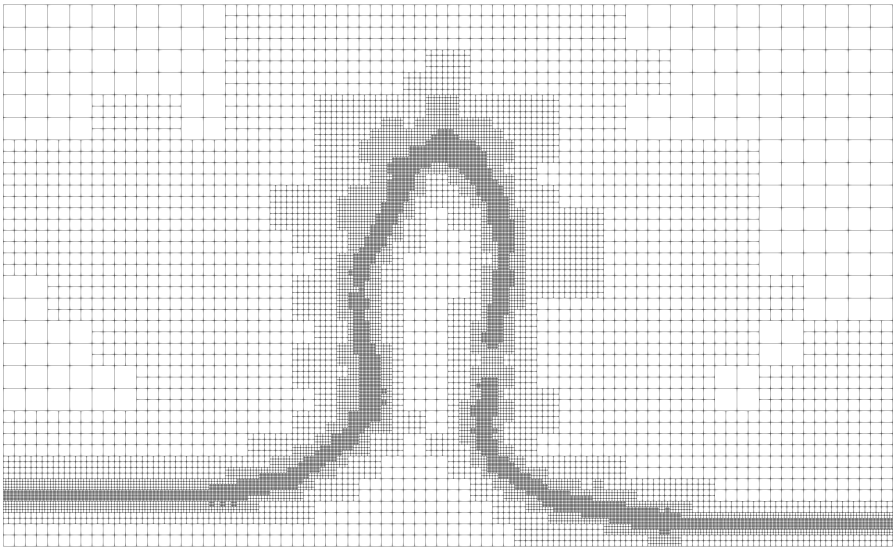

Figure 12. Adaptively refined grid for the first time step of the simulation. We can see that the grid is refined to a high level at the interface between the salt and the sediment overburden, where the highest velocity gradients appear. On the contrary, it is coarsened where the velocity has small gradients, particularly in the upper right and upper left corners.

the deposition of the sediments at the same time as the formation of the diapir, by removing the sediment layers one by one. For simplification purposes and in order to test the process with simple boundary conditions, such sedimentation processes were not implemented, which explains the presence of the weld. The results are, however, quite convincing despite the high level of simplification. The analysis of the five experiments shows that in this setup, the viscosity contrast between salt and sediment and the density of the sediments do not have a big impact on the shape of the model after the restoration process. Only the shape of the sediments at the base of the diapir is slightly different from one experiment to the other. Experiments 4 and 5 have serrated shapes that are not geologically probable, probably because of the four orders of magnitude of viscosity contrast between the salt and sediments. The main difference between the experiments is the relaxation time for each restoration process. If the duration of the formation of the diapir was known, it could then be used to reduce the uncertainty on which density and viscosity to use.

5 Discussion

While the results of the three test models in the previous section are promising, their purpose is not to correctly compute the deformation of the subsurface in a forward mechanical simulation, but rather to assess the validity of the proposed restoration scheme and the underlying concepts. As such, their setup is allowed to be a strong simplification of what would lead to the formation of a salt diapir in natural circumstances. Indeed, research on the formation of salt structures shows that extensional

https://doi.org/10.5194/se-2020-89
Preprint. Discussion started: 27 May 2020

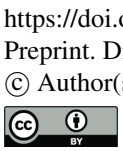

Solid Earth
Discussions
Open Access
EGU

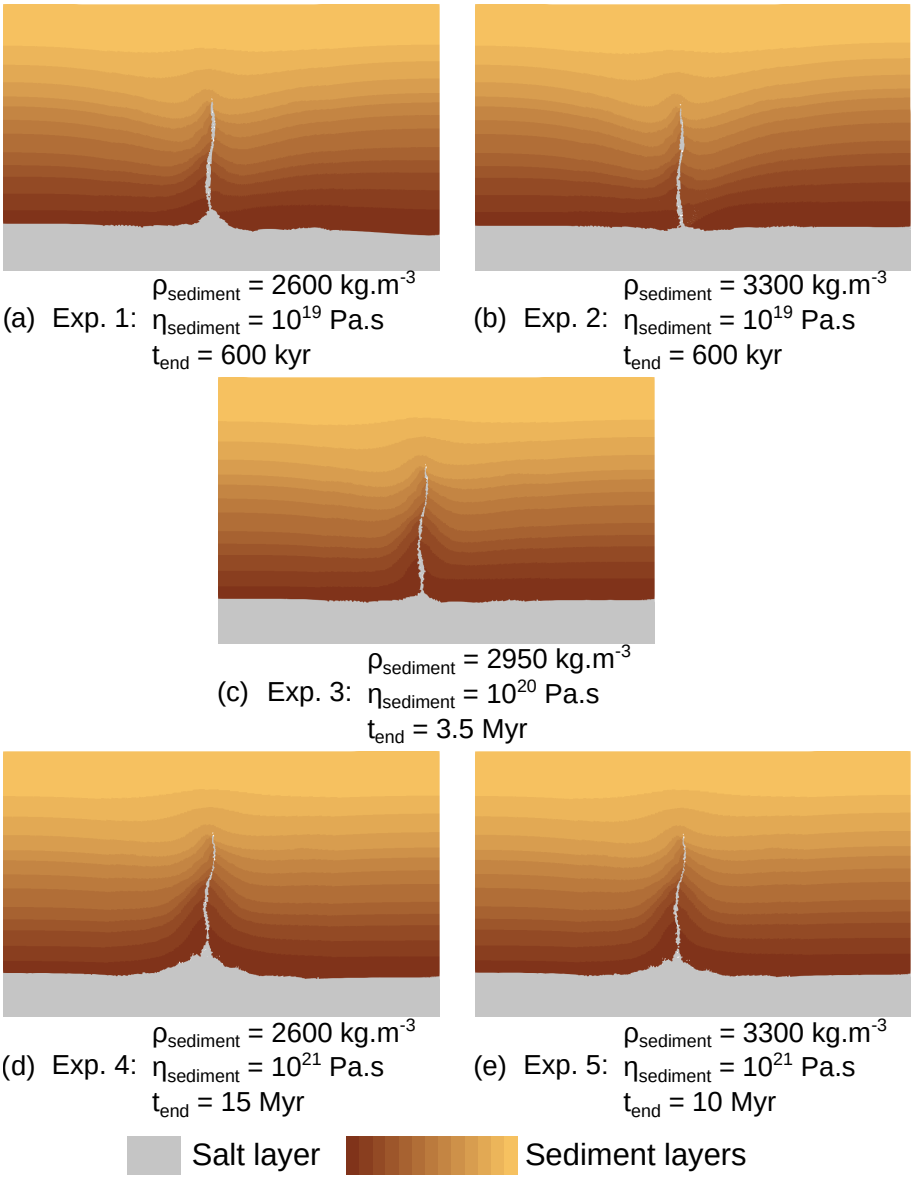

Figure 13. Results of the 5 restoration experiments done on the salt model setup of Fig. 11, after different time spans t_{end}.

and compressional contexts, and especially faults within them, as well as differential deposition loading, are a leading factor for most kinds of diapirism (e.g., Jackson and Hudec, 2017). The use of a Newtonian rheology for the overburden and salt also simplifies the highly complex visco-elasto-plastic behavior of rocks (e.g., Hughes and Taylor, 1978; Gerbault et al., 1998; Cornet, 2015).

300 The main interest of the proposed restoration scheme is the change of the deformation drive compared to previous methods of geomechanical restoration, which usually rely on flattening the top surface of the horizons (e.g., Guzofski et al., 2009;

https://doi.org/10.5194/se-2020-89
Preprint. Discussion started: 27 May 2020

Lovely et al., 2012; Chauvin et al., 2018), and may lead to unphysical strains. Here the deformation is driven by the density contrasts in the model and by the boundary conditions. As such, more physical strains are expected, given that the boundary conditions and the rheology inside the model are close enough to reality. This implies two important questions when applying a reverse-time Stokes restoration scheme: what are the material properties of the geological objects inside the model, and what type and intensity of boundary conditions should be applied to these geological objects? Regarding the material properties, the diapir test model of Sect. 4.3 gave a first idea of how to choose them. The density of the subsurface depends on the type of rocks that are present, and its estimation is relatively easy. The viscosity, however, is not trivial, as laboratory observation time scales are too short to reflect the slow movement occuring at geological time scales. The values we took are inspired from numerical simulations, but they have a large uncertainty (at least one order of magnitude) (e.g., Massimi et al., 2006; Kronbichler et al., 2012), as they are calibrated using postglacial rebound data for example. Works on analog sandbox experiments and further experiments on models with more geological knowledge should prove to be useful in estimating a proper viscosity for the restoration of different rock rheologies. In particular, the duration over which the geologic phenomena occur should guide the choice of viscosity values in subsurface models. Regarding the rheology of faults, we cannot directly use their usual forward modeling implementation considering the rock as having a plastic behavior. Indeed, the previous stress history is needed to simulate such a behavior, and it is not available in restoration, which studies backward movement. Using a specific viscosity for the implementation of faults in restoration can, however, be considered and holds two advantages. First, since all the faults are already identified at the beginning of the restoration process, we do not need to allow the creation of faults in backward simulations. Second, using an effective viscosity for the faults would allow for a more realistic simulation of shear band and damage zone behavior, compared to previous geomechanical restoration schemes that consider faults as free-slip surfaces.

A significant issue with the boundary conditions in geomechanical simulations is the difficulty to estimate the paleo-forces at play several kilometers underground. We therefore need to choose Dirichlet and Neumann boundary conditions that best fit the tectonic knowledge about the region of study. In the test models presented in the previous section, the boundary conditions are either free-slip or no-slip, which is a strong simplification of reality. For example, deformation is generally strongly influenced by the horizontal stress state, implying compressive or extensive structures and the need for corresponding conditions on the side boundaries (Chauvin et al., 2018). Another example is the top surface of the model in Sect. 4.2, which can be considered as being on ground level, and is therefore in contact with air. This interface is complicated to handle due to the several orders of magnitude in the material property contrast (very high density and viscosity for rocks versus very low density and viscosity for the air). In geomechanical simulations, several approaches exist to model its behavior. The simplest topographic surface solution is to set a free-slip condition which removes the normal component of the velocity at the boundary. This simplification is mostly used in cases where the movement of the top surface is negligible compared to the rest of the model. In order to do more realistic simulations, two main approaches are available: the implementation of a free surface, or the "sticky air" method (e.g., Crameri et al., 2012, for a benchmark and a comparison of the two methods). The sticky air method considers a layer of material with a low viscosity and zero density, the difficulty being that this viscosity needs to be sufficiently low to be negligible compared to the rest of the model, but high enough for the solvers to converge. The free surface method considers that no force is applied on the surface of the computational mesh. While this is theoretically simple, it is numerically

https://doi.org/10.5194/se-2020-89
Preprint. Discussion started: 27 May 2020

complicated to implement, as it also means that the computational mesh needs to honor the movement of the free surface. In FAIStokes, the free surface method is applied by tracking the movement of the top surface and allowing the grid nodes to move vertically (Appendix. D). In order to stabilize its movement and avoid some of the instabilities that can appear, the free surface stabilization algorithm (refered to as FSSA in the rest of the paper) presented in Kaus et al. (2010) has been implemented. The free surface implementation has been benchmarked and performs well in forward simulations (Appendices E and F). However, in restoration simulations of models where the only drive is a density contrast (such as the models shown in the previous section), the free surface is unstable. This appears particularly when working with models that have a near-horizontal or initially horizontal top surface such as the one presented in Fig. 7. In those setups, any small computational error in the computation of the vertical part of the velocity can lead to instabilities that increase exponentially in reverse time. Several approaches involving specific tractions on the top surface have been tested to remove or correct this instability, but we have not yet devised any efficient means to prevent this. In particular, the FSSA delays this phenomenon, but does not suppress it altogether. We hope, however, that this instability issue will be reduced by adding more geological relevance to the simulation in the form of other components to the drive of the simulation, such as faults and extensive/compressive boundary conditions.

6 Conclusions

We have presented a new scheme that exploits the reversibility of Stokes flow equations to perform structural restoration. While this does not tackle all the issues with the current geomechanical restoration implementations, it improves some of their aspects, such as the replacement of the Dirichlet boundary condition on the top surface by a "natural" body force to drive the reverse deformation, and the use of viscous behavior. The FAIStokes code was developed to apply this restoration scheme and allow various tests on its implementation. Among those tests, we presented three simple models and the results we obtained with them. Those results are encouraging, although the numerical method has difficulties dealing with the restoration of salt in the presence of welds. The free surface also leads to instabilities in the restoration process which have not been dealt with in an efficient way yet.

We intend to follow this work by applying the method to more complex models, starting with the restoration of sandbox experiments (e.g., Colletta et al., 1991). This will allow us to add more physical boundary conditions, specific implementations of faults, and to do more precise tests on the value to choose for the viscosity and density of geological layers.

Code availability. The code corresponding to this paper is available to members of the RING consortium in the FAIStokes software. The FE parts of the code, however, come from the open source library deal.II. This library is also used in the open source software ASPECT, which also allows the use of PIC and FSSA.

Video supplement. For a video example of the restoration of the upscaled van Keken model, viewers can go to https://doi.org/10.5446/46388

https://doi.org/10.5194/se-2020-89
Preprint. Discussion started: 27 May 2020

Solid Earth
Discussions
Open Access
EGU

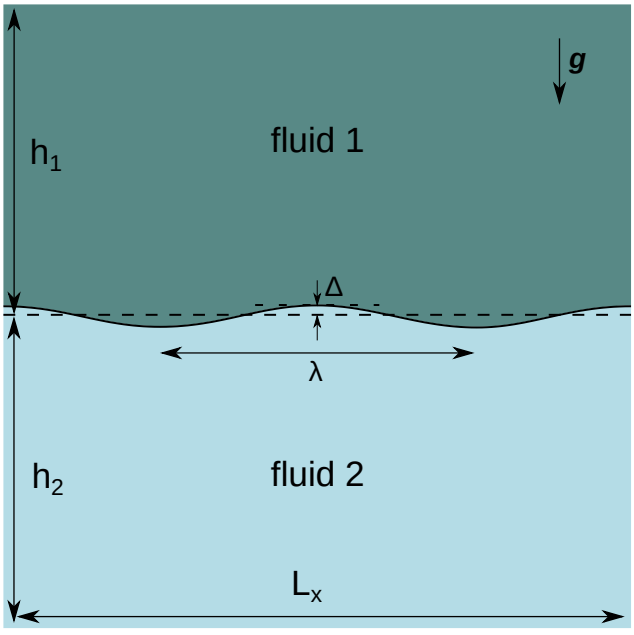

Figure A1. Rayleigh-Taylor instability benchmark initial setup.

Appendix A: Taking into account small scales inside a model : the Rayleigh-Taylor instability benchmark

This benchmark is based on the analytical solution of a Rayleigh-Taylor instability by Ramberg (1968) and was carried out in various numerical studies (Deubelbeiss and Kaus (2008); Thieulot (2011)). It consists of a two-layer system driven by gravity, the density of the bottom layer being smaller. The bottom and top boundaries have a no slip boundary condition, while the sides have a free slip boundary condition.

The first layer, made of fluid 1 with properties (ρ_1, η_1), overlays the second layer, made of fluid 2 (ρ_2, η_2). An initial sinusoidal disturbance of the interface between the two layers is introduced, characterized by an amplitude Δ and a wavelength λ, as shown in Fig. A1.

Under these conditions, the velocity of the diapiric growth v is given by Ramberg (1968):

$$\frac{v}{\Delta} = -K \frac{\rho_1 - \rho_2}{2\eta_2} h_2 g \tag{A1}$$

with K the dimensionless growth factor given by

$$K = \frac{-d_{12}}{c_{11} j_{22} - d_{12} i_{21}} \tag{A2}$$

https://doi.org/10.5194/se-2020-89
Preprint. Discussion started: 27 May 2020

Solid Earth
Discussions
Open Access
EGU

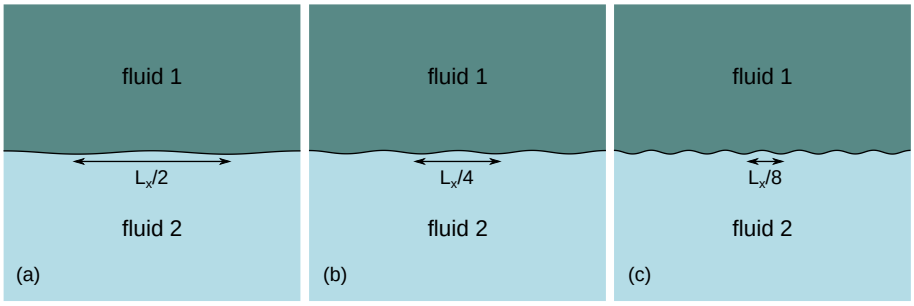

Figure A2. Initial setup of the Rayleigh-Taylor instability benchmark with 3 different wavelength: a) $\lambda = L_x/2$, b) $\lambda = L_x/4$, c) $\lambda = L_x/8$

which involves the following factors:

$$
\begin{aligned}
\phi_1 &= \frac{2\pi h_1}{\lambda} \\
\phi_2 &= \frac{2\pi h_2}{\lambda} \\
c_{11} &= \frac{2\eta_1\phi_1^2}{\eta_2(\cosh(2\phi_1)-1-2\phi_1^2)} - \frac{2\phi_2^2}{\cosh(2\phi_2)-1-2\phi_2^2} \\
d_{12} &= \frac{\eta_1(\sinh(2\phi_1)-2\phi_1)}{\eta_2(\cosh(2\phi_1)-1-2\phi_1^2)} + \frac{\sinh(2\phi_2)-2\phi_2}{\cosh(2\phi_2)-1-2\phi_2^2} \\
i_{21} &= \frac{\eta_1\phi_2(\sinh(2\phi_1)+2\phi_1)}{\eta_2(\cosh(2\phi_1)-1-2\phi_1^2)} + \frac{\phi_2(\sinh(2\phi_2)+2\phi_2)}{\cosh(2\phi_2)-1-2\phi_2^2} \\
j_{22} &= \frac{2\eta_1\phi_1^2\phi_2}{\eta_2(\cosh(2\phi_1)-1-2\phi_1^2)} - \frac{2\phi_2^3}{\cosh(2\phi_2)-1-2\phi_2^2}
\end{aligned}
\tag{A3}
$$

We set $\rho_1 = 3300$ kg.m^{-3}, $\rho_2 = 3000$ kg.m^{-3}, $\eta_1 = 10^{21}$ Pa.s, $L_x = h_1 + h_2 = 512$ km, and $\Delta = 3$ km. We make η_2 vary between 1.25×10^{20} and 2.5×10^{23} Pa.s, while λ takes three values: $L_x/2, L_x/4, L_x/8$ (Fig. A2).

A first run is done, where the FEM grid is fixed to 80×80 elements, each containing 10^2 regularly spaced particles. In order to test the influence of adaptive refinement, we conduct a second run with a grid starting at 80×80 elements and three levels of adaptive refinement. We also refine the particle swarm adaptively: each initial cell is first filled with 5^2 regularly spaced particles, and then the swarm is densified to 64 times more particles around the interface between the two fluids. The results are shown along with the analytical ones in Fig. A3.

Overall, results show a good agreement between the computed solution and the reference, especially in the case of adaptive refinement, where the relative error falls beneath 2.5% for all the curves. Since ϕ_1 is inversely proportional to the wavelength λ, it means that the code can account well for small disturbances, especially with the use of adaptive refinement on the parts with higher velocity and high contrasts in viscosity.

This benchmark ensures the validity of the code in the presence of large viscosity constrasts, even if those constrasts are located on deformations that are small compared to the size of the model. It also validates the averaging of the density and viscosity from the particles to the finite element grid.

https://doi.org/10.5194/se-2020-89
Preprint. Discussion started: 27 May 2020

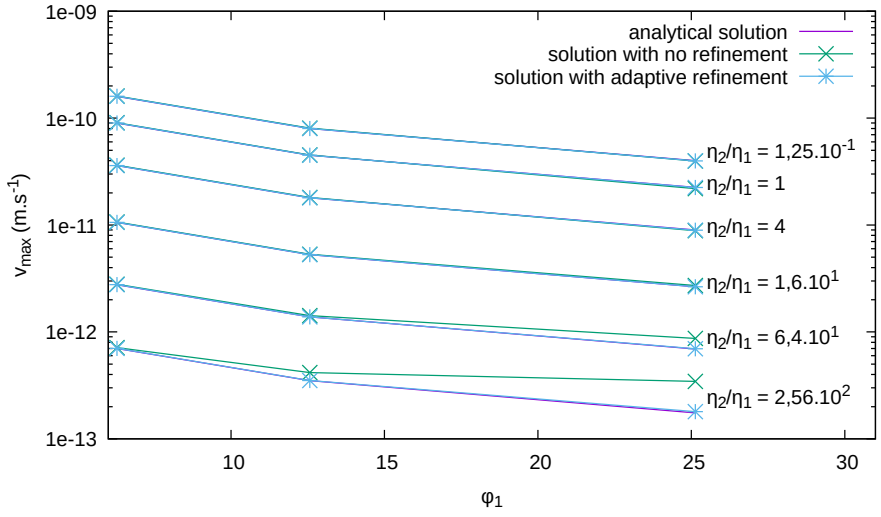

Figure A3. Comparison between numerical and analytical results for the Rayleigh-Taylor instability benchmark. The numerical results are computed for a 80×80 element grid and for the same grid with three levels of adaptive refinement.

Appendix B: Taking into account viscosity changes : the falling block benchmark

This benchmark appears in Gerya (2019) and is presented in Thieulot (2011). It consists in modelling the fall of a block of fluid of properties (ρ_1, η_1) inside another fluid of properties (ρ_2, η_2), with $\rho_1 > \rho_2$. The domain is a square of size $L_x = L_y = 500$ km, and the block (a square in 2D) of size 100×100 km is initially centered at point ($x = 250$ km, $y = 400$ km), as shown in Fig. B1.

The simulation is carried out on a 50×50 element grid that is adaptively refined three times. Like in the previous benchmark, the particle swarm is created by first introducing 5^2 particles in each initial element, and then densifying it up to 64 times more particles around the zone of interest (i.e. the falling block). Free slip boundary conditions are imposed on all sides of the domain. We carry out five experiments:

- Exp.1: $\eta_2 = 10^{20}$ Pa.s, $\rho_1 = 3220$ kg.m^{-3};
- Exp.2: $\eta_2 = 10^{21}$ Pa.s, $\rho_1 = 3300$ kg.m^{-3};
- Exp.3: $\eta_2 = 10^{22}$ Pa.s, $\rho_1 = 6600$ kg.m^{-3};
- Exp.4: $\eta_2 = 10^{23}$ Pa.s, $\rho_1 = 3300$ kg.m^{-3};
- Exp.5: $\eta_2 = 10^{24}$ Pa.s, $\rho_1 = 9900$ kg.m^{-3};

In all the experiments, the density of the surrounding fluid is $\rho_2 = 3200$ kg.m^{-3} and the viscosity of the block is varied between 10^{19} and 5×10^{27} Pa.s. The velocity of the falling block is measured in its centre at $t = 0$ for all experiments.

https://doi.org/10.5194/se-2020-89
Preprint. Discussion started: 27 May 2020

Solid Earth
Discussions
Open Access
EGU

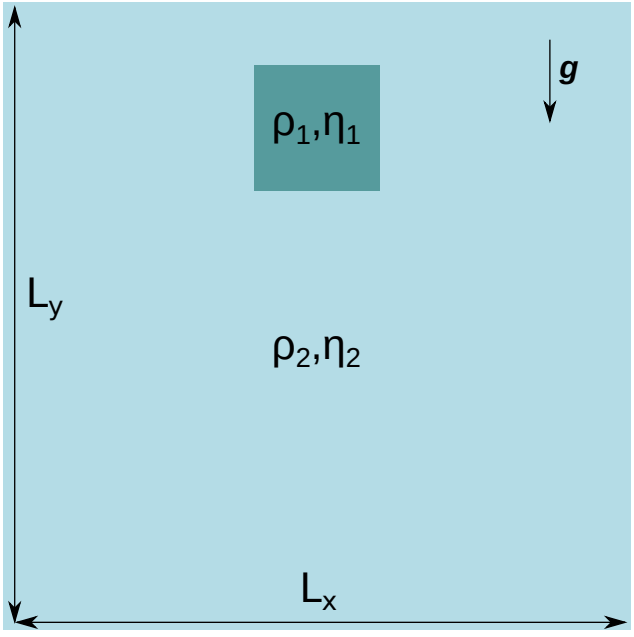

Figure B1. Falling block benchmark initial setup.

Following physical intuition, one expects the velocity of the block to act as follows: (a) decrease when the viscosity of the surrounding fluid η_2 increases (i.e. when going from Exp.1 to Exp.5), and (b) increase with the density contrast $(\rho_1 - \rho_2)$ in each experiment. To check this behavior, we measure $v\eta_2/(\rho_1 - \rho_2)$ as a function of the viscosity contrast $\log_{10}(\eta_2/\eta_1)$. The results of the benchmark are plotted in Fig. B2.

We can see that the experimental points line up on a single curve, which shows that FAIStokes can deal with gravity-driven simulations where $0.6\% \leq (\rho_1 - \rho_2)/\rho_2 \leq 210\%$ and the viscosity contrasts are as strong as $10^{-6} \leq \eta_2/\eta_1 \leq 10^5$ in a consistent manner.

Appendix C: Advecting particles : the rotation benchmark

The last benchmark aims at assessing the error in the advection part only. The setup of the model is a square of size 10×10 km, where we study the advection of a single particle, starting at coordinates $(8\ \mathrm{km}, 5\ \mathrm{km})$ and doing a 2π rotation around the center point $(5\ \mathrm{km}, 5\ \mathrm{km})$ (Fig. C1). A velocity field is prescribed in the domain and discretized on the grid: on each grid point, the velocity has a constant norm and is always normal to the line connecting the point to the model center:

$$\boldsymbol{v} = v_0.\boldsymbol{e_\theta} = \begin{pmatrix} v_0.sin\theta \\ v_0.cos\theta \end{pmatrix} \tag{C1}$$

The grid is not adaptively refined here, and is composed of 16×16 elements. In order to have scales that are geologically relevant, we choose $v_0 = 3\ \mathrm{cm.year}^{-1}$ and vary the time step Δt between 500 and 2000 years (in this setup, the CFL numbers

https://doi.org/10.5194/se-2020-89
Preprint. Discussion started: 27 May 2020

Solid Earth
Discussions
Open Access
EGU

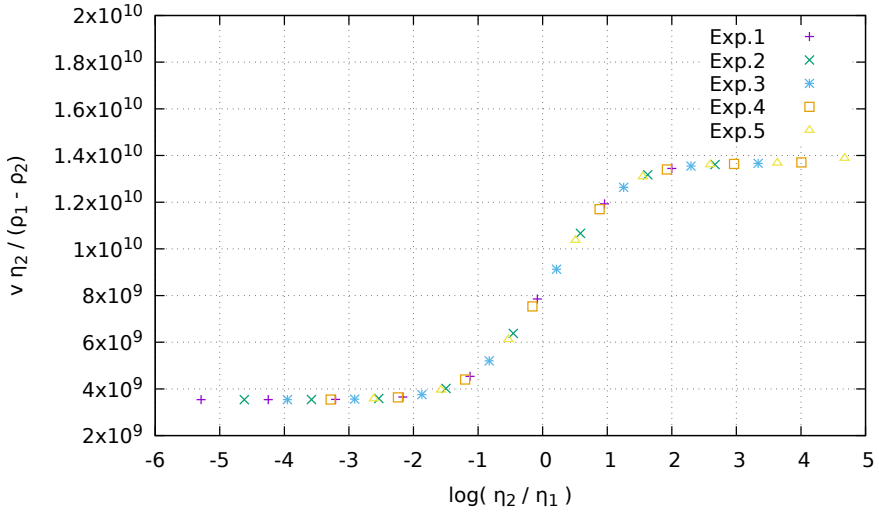

Figure B2. Velocity measurements as a function of the viscosity contrast between surrounding medium and block for the experiments of the falling block benchmark.

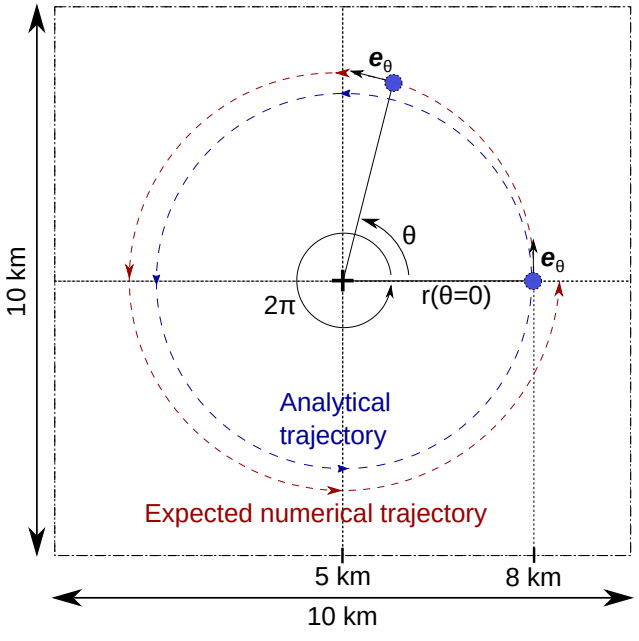

Figure C1. Setup for the rotation benchmark, assessing errors on the advection of particles.

chosen for our simulations would give a timestep between 175 years for the lowest CFL number and 1753 years for the highest CFL number). The second order Runge-Kutta scheme presented in Sect. 3.6 is used at all time steps. We then evaluate

https://doi.org/10.5194/se-2020-89
Preprint. Discussion started: 27 May 2020

Solid Earth
Discussions
Open Access
EGU

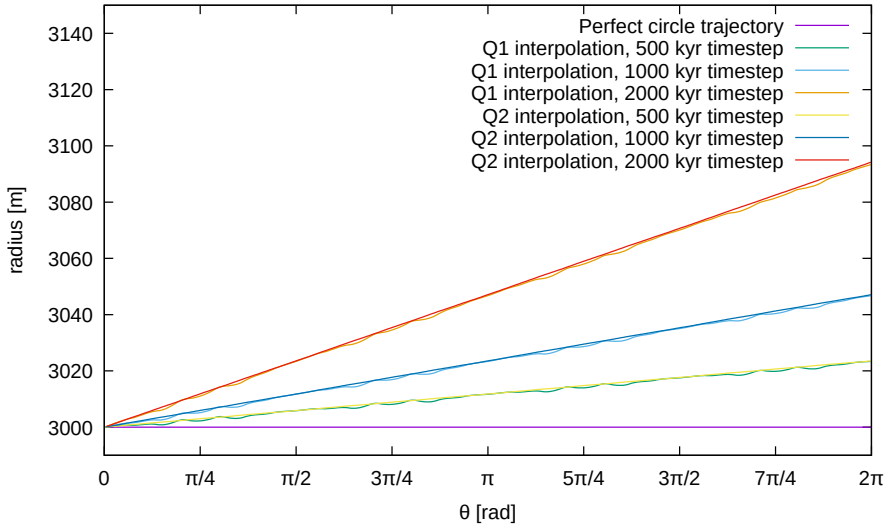

Figure C2. Results for the rotation benchmark obtained with different time steps and advection schemes.

the distance $\Delta r = |r(\theta = 0) - r(\theta = 2\pi)|$. This distance gives us a measure of the error made in the computation of the particle advection, and allow us to compare different advection schemes. Figure C2 shows the results obtained for a 2π rotation of the particle with different interpolation schemes. We can see that reducing the timestep linearly reduces the error on the radius $r(\theta)$. In this setup, the type of interpolation mostly impacts the stability of the interpolation, and not the accuracy.

Appendix D: Free surface implementation

In the case of a free surface on the top of the model, the top surface is tracked by a separate point swarm. This point swarm is denser than the material particle swarm and is 1 dimension lower (i.e. a line in our 2D cases). It is advected at each time step the same way as the particle swarm that represents the geological model. After its displacement or during the setup of the grid, the free surface point swarm is used as a reference to move vertically the nodes of the grid at the top of the model, so that they match the free surface. This vertical displacement is then propagated to the rest of the grid so that the grid cells stay as close to squares as possible, while not affecting the other boundaries. Fig. D1 illustrates the whole process. Since our models are isothermal no special processing is required here to correct the temperature field during this process. Appendix E shows the results of a benchmark that tests the free surface implementation along with other computational parts of the code. The free surface stabilization algorithm developed by Kaus et al. (2010) and Quinquis et al. (2011) has been implemented in FAIStokes; we benchmark it in Appendix F.

https://doi.org/10.5194/se-2020-89
Preprint. Discussion started: 27 May 2020

Solid Earth
Discussions
Open Access
EGU

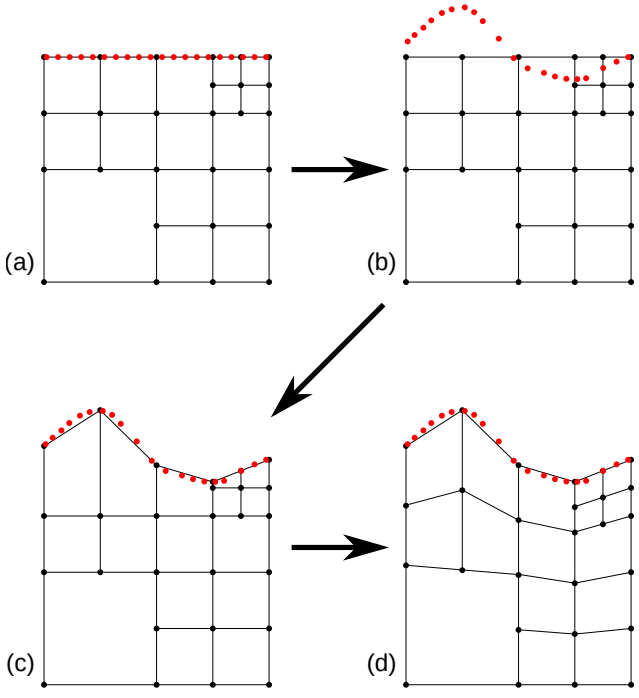

Figure D1. Update of the free surface: (a) Initial state where the velocity is computed on the grid. (b) The point swarm tracking the free surface is advected according to the computed velocity. (c) The grid nodes at the top of the free surface are moved vertically to match the point swarm. (d) The deformation of the grid is diffused to the rest of the nodes.

Appendix E: Taking into account the top surface in contact with air : the free surface benchmark

This benchmark is presented in Crameri et al. (2012), where it is applied on several numerical codes to compare their implementation of the free surface, and evaluate the use of the 'sticky air' method. It will be used here to evaluate the quality of our approximation and interpolation of the free surface. It consists on a cosine-shaped layer of homogeneous lithosphere overlaying a homogeneous layer of mantle. For this type of model, Ramberg (1981) gives an analytical solution for the maximal height of the topography at each time t :

$$h_{analytical}(t) = h_{initial}\ \exp(-\gamma t) \tag{E1}$$

where γ is the relaxation rate and $h_{initial}$ is the value of h at the beginning of the simulation. The model setup for the benchmark is shown in Fig. E1.

The bounding box of the model spans 2800 km by 707 km. The underlaying mantle layer is 600 km thick, while the lithosphere has a thickness between 93 and 107 km. The lithosphere's top surface is cosine-shaped with an amplitude of 7 km and a wavelength of the size of the domain. The mantle and lithosphere have a density of $\rho_M = \rho_L = 3300$ kg.m^{-3} and a viscosity of $\eta_M = 10^{21}$ Pa.s and $\eta_L = 10^{23}$ Pa.s, respectively. We set free slip boundary conditions for the sides and a no slip condition on the bottom of the model. The initial grid is made of 16×64 elements and is adaptively refined 3 times. The particle

https://doi.org/10.5194/se-2020-89
Preprint. Discussion started: 27 May 2020

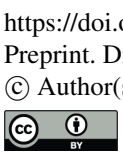

Solid Earth
Discussions
Open Access
EGU

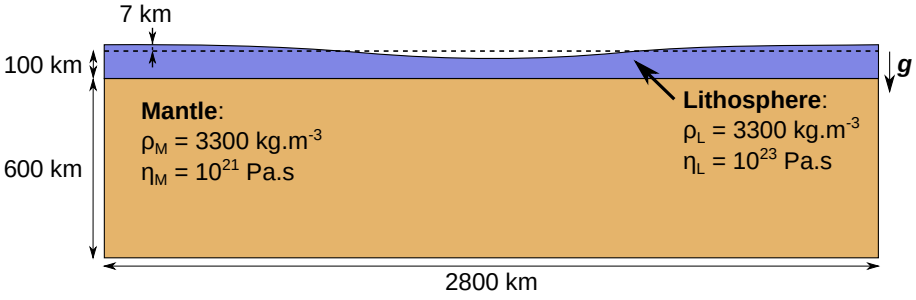

Figure E1. Model setup for the 2D free surface benchmark.

swarm contains $484,160$ particles; it is constructed by first sampling regularly the domain, and then adaptively densifying the swarm to 64 times more particles in the lithosphere and upper part of the mantle. In this setup, Crameri et al. (2012) gives a characteristic relaxation rate $\gamma = 0.2139 \times 10^{-11}$ s^{-1} and a characteristic relaxation time $t_{relax} = 14.825 \times 10^3$ year. The results obtained with FAIStokes are given in Fig. E2.

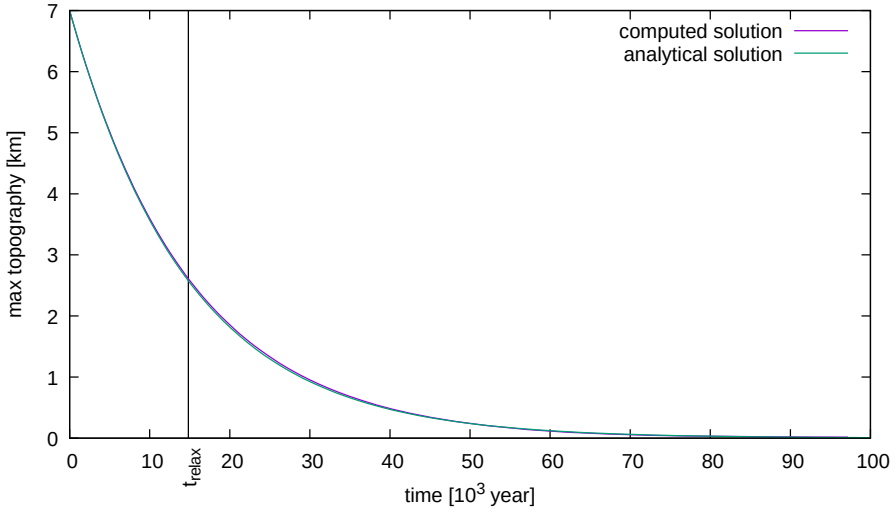

Figure E2. Comparison between the analytical and numerical results of the maximum topography over time for the free surface benchmark.

The numerical results are close to the analytical ones, with only a 1.3% error at the characteristic relaxation time. This shows the capacity of FAIStokes to compute the solution of Stokes equations with a free surface for small vertical deformation, and to advect the particles inside the model. It also gives another evaluation of the handling of gravity-driven flow, this time with the addition of evolution inside the model.

https://doi.org/10.5194/se-2020-89
Preprint. Discussion started: 27 May 2020

Solid Earth
Discussions
Open Access
EGU

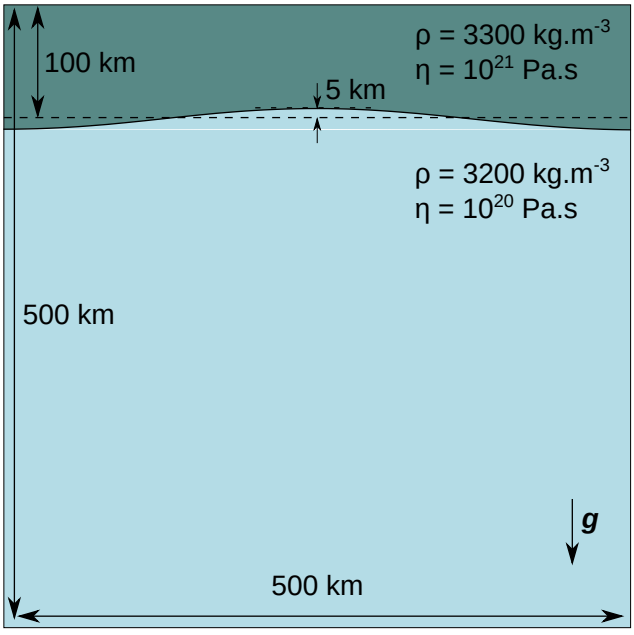

Figure F1. Sloshing free surface benchmark initial setup.

Appendix F: Upgrading the free surface movement : the sloshing benchmark

This benchmark is presented in Kaus et al. (2010), where it is used to assess the results of the free surface stabilization algorithm (FSSA) presented in the same article. It is used here to verify the implementation of the same algorithm in our code, as well as check the behavior of the free surface in another setup. The benchmark model is another Rayleigh-Taylor instability with a dense, more viscous layer sinking into a less dense fluid (Fig. F1).

The model span is $500\ \mathrm{km} \times 500\ \mathrm{km}$; the side boundaries have a free-slip condition, the lower boundary is no-slip, and the top boundary is a free surface. The initial perturbation between the two layers is sinusoidal with an amplitude of $5\ \mathrm{km}$. The computation is carried out on a grid with 25×25 initial elements and three adaptive refinement steps. The particle swarm counts $25,000$ particles; it is constructed by first sampling regularly the model and then densifying it to 64 times more particles around the interface. The specificity of this benchmark is the apparition of a sloshing instability (also refered to as the "drunken sailor" instability) if the simulation time step is too large. Specifically here, without the FSSA, the forward simulation is stable with a time step Δt of $2500\ \mathrm{years}$, but with $\Delta t = 5000\ \mathrm{years}$, an instability emerges as the velocity pattern changes direction from one time step to the other (Fig F2).

In order to follow the evolution of the free surface, we keep trace of the altitude of the most top-left point over time. Results of a $0.5\ \mathrm{Myr}$ simulation, for different time steps Δt, with and without the FSSA, are shown in Fig. F3. We can see that the implementation of the FSSA stabilizes the sloshing behavior of the free surface that appeared whith a time step Δt of $5000\ \mathrm{years}$, and keeps the free surface stable even with higher time steps. Moreover, the results show great similarities

https://doi.org/10.5194/se-2020-89
Preprint. Discussion started: 27 May 2020

Solid Earth
Discussions
Open Access
EGU

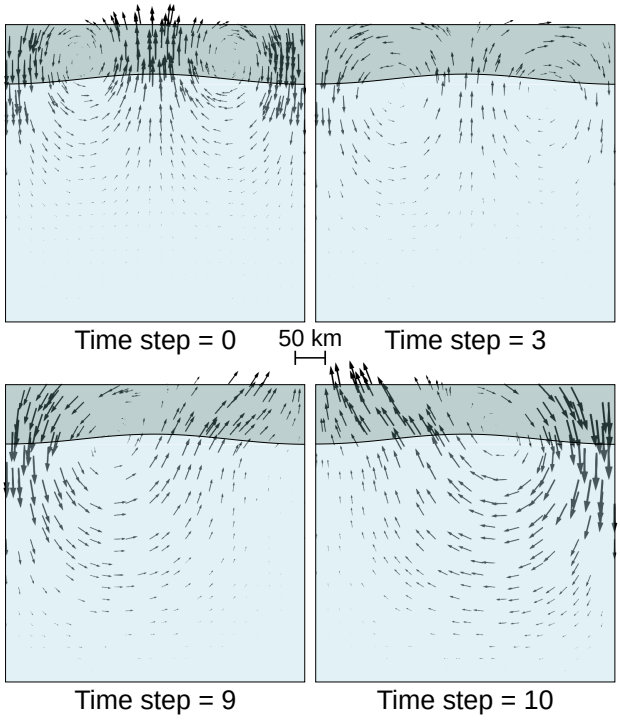

Figure F2. Simulation evolution for $\Delta t = 5000$ years, showing the sloshing instability: the velocity pattern changes from one time step to the other, the velocity norm increasing each time.

to those that can be found in Kaus et al. (2010) and Thieulot (2019). This validates the implementation of the free surface stabilization algorithm. It also gives another evaluation of the handling of gravity-driven flow with a free surface, this time with the additional resolution of an instability that can occur with free surfaces.

Author contributions. The writing of this paper, as well as the code of the software and the results, was done by M S-S. CT helped with useful discussions and new points of view on the subject of the paper, as well as help on the code structure, benchmarks, and methods. GC and PC provided useful discussions on the subject, guidance on solving the different problems, and funding for the PhD thesis that allowed this research through the RING-Gocad consortium. All authors contributed to the conceptualization, the design of experiments and the analysis of results. CT, GC and PC also helped on the manuscript with useful feedback and corrections.

Competing interests. The authors declare that they have no conflict of interests.

https://doi.org/10.5194/se-2020-89
Preprint. Discussion started: 27 May 2020

Solid Earth
Discussions
Open Access
EGU

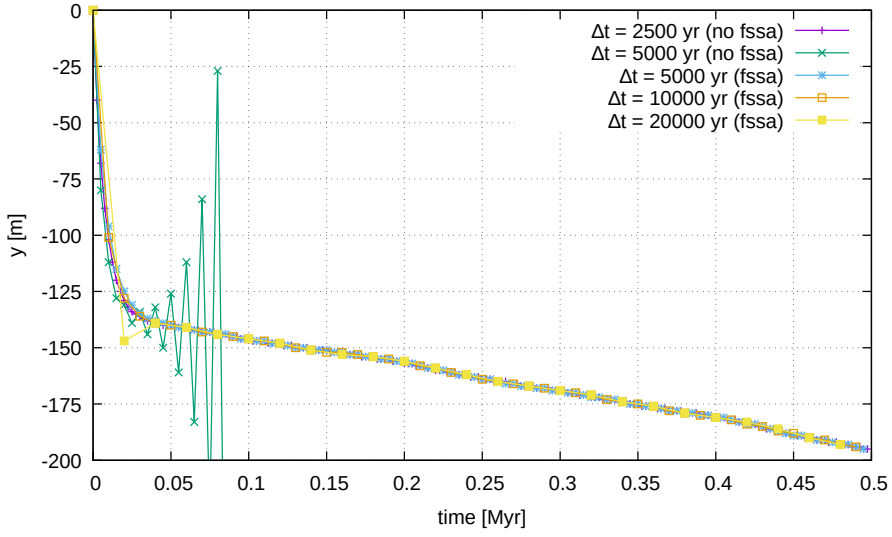

Figure F3. Altitude of the most top-left point of the grid over time, for the sloshing free surface benchmark, for diffent time steps with and without the FSSA.

Acknowledgements. This project was done in the frame of the RING project, in the GeoRessources laboratory. We would like to thank for their support the academic and industrial sponsors of the RING-GOCAD Consortium managed by ASGA (https://www.ring-team.org/consortium). We would also like to thank Jean Braun for valuable discussions and suggestions on this work.

https://doi.org/10.5194/se-2020-89
Preprint. Discussion started: 27 May 2020

References

Al-Fahmi, M. M., Plesch, A., Shaw, J. H., and Cole, J. C.: Restorations of faulted domes, AAPG Bulletin, 100, 151–163, 2016.

Allen, P. A. and Allen, J. R.: Basin analysis: Principles and application to petroleum play assessment, John Wiley & Sons, 2013.

Anquez, P., Pellerin, J., Irakarama, M., Cupillard, P., Lévy, B., and Caumon, G.: Automatic correction and simplification of geological maps and cross-sections for numerical simulations, Comptes Rendus Geoscience, 351, 48–58, 2019.

Arndt, D., Bangerth, W., Clevenger, T. C., Davydov, D., Fehling, M., Garcia-Sanchez, D., Harper, G., Heister, T., Heltai, L., Kronbichler, M., Kynch, R. M., Maier, M., Pelteret, J.-P., Turcksin, B., and Wells, D.: The `deal.II` Library, Version 9.1, Journal of Numerical Mathematics, https://doi.org/10.1515/jnma-2019-0064, https://dealii.org/deal91-preprint.pdf, accepted, 2019.

Arndt, D., Bangerth, W., Davydov, D., Heister, T., Heltai, L., Kronbichler, M., Maier, M., Pelteret, J.-P., Turcksin, B., and Wells, D.: The deal. II finite element library: Design, features, and insights, Computers & Mathematics with Applications, https://doi.org/https://doi.org/10.1016/j.camwa.2020.02.022, 2020.

Asgari, A. and Moresi, L.: Multiscale Particle-In-Cell Method: From Fluid to Solid Mechanics, in: Advanced Methods for Practical Applications in Fluid Mechanics, edited by Jones, S. A., chap. 9, IntechOpen, Rijeka, https://doi.org/10.5772/26419, https://doi.org/10.5772/26419, 2012.

Athy, L. F.: Density, porosity, and compaction of sedimentary rocks, AAPG Bulletin, 14, 1–24, 1930.

Bangerth, W., Hartmann, R., and Kanschat, G.: deal.II – a General Purpose Object Oriented Finite Element Library, ACM Trans. Math. Softw., 33, 24/1–24/27, 2007.

Bouziat, A., Guy, N., Frey, J., Colombo, D., Colin, P., Cacas-Stentz, M.-C., and Cornu, T.: An Assessment of Stress States in Passive Margin Sediments: Iterative Hydro-Mechanical Simulations on Basin Models and Implications for Rock Failure Predictions, Geosciences, 9, 469, 2019.

Braun, J.: Pecube: A new finite-element code to solve the 3D heat transport equation including the effects of a time-varying, finite amplitude surface topography, Computers & Geosciences, 29, 787–794, 2003.

Chamberlin, R. T.: The Appalachian folds of central Pennsylvania, The Journal of Geology, 18, 228–251, 1910.

Chauvin, B. P., Lovely, P. J., Stockmeyer, J. M., Plesch, A., Caumon, G., and Shaw, J. H.: Validating novel boundary conditions for three-dimensional mechanics-based restoration: An extensional sandbox model example, AAPG Bulletin, 102, 245–266, 2018.

Clausolles, N., Collon, P., and Caumon, G.: Generating variable shapes of salt geobodies from seismic images and prior geological knowledge, Interpretation, 7, T829–T841, 2019.

Cobbold, P. R. and Percevault, M.-N.: Spatial integration of strains using finite elements, in: Strain Patterns in Rocks, pp. 299–305, Elsevier, 1983.

Colletta, B., Letouzey, J., Pinedo, R., Ballard, J. F., and Balé, P.: Computerized X-ray tomography analysis of sandbox models: Examples of thin-skinned thrust systems, Geology, 19, 1063–1067, 1991.

Cornet, F. H.: Elements of crustal geomechanics, Cambridge University Press, 2015.

Crameri, F., Schmeling, H., Golabek, G., Duretz, T., Orendt, R., Buiter, S., May, D., Kaus, B., Gerya, T., and Tackley, P.: A comparison of numerical surface topography calculations in geodynamic modelling: an evaluation of the 'sticky air' method, Geophysical Journal International, 189, 38–54, 2012.

Dahlstrom, C.: Balanced cross sections, Canadian Journal of Earth Sciences, 6, 743–757, 1969.

https://doi.org/10.5194/se-2020-89
Preprint. Discussion started: 27 May 2020

De Santi, M. R., Campos, J. L. E., and Martha, L. F.: A Finite Element approach for geological section reconstruction, in: Proceedings of the 22th Gocad Meeting, Nancy, France, pp. 1–13, Citeseer, 2002.

Deubelbeiss, Y. and Kaus, B.: Comparison of Eulerian and Lagrangian numerical techniques for the Stokes equations in the presence of strongly varying viscosity, Physics of the Earth and Planetary Interiors, 171, 92–111, 2008.

Dimakis, P., Braathen, B. I., Faleide, J. I., Elverhøi, A., and Gudlaugsson, S. T.: Cenozoic erosion and the preglacial uplift of the Svalbard–Barents Sea region, Tectonophysics, 300, 311–327, 1998.

Donea, J., Huerta, A., Ponthot, J.-P., and Rodriguez-Ferran, A.: Arbitrary Lagrangian-Eulerian Methods, volume 1 of Encyclopedia of Computational Mechanics, chapter 14, John Wiley & Sons Ltd, 3, 1–25, 2004.

Durand-Riard, P., Caumon, G., and Muron, P.: Balanced restoration of geological volumes with relaxed meshing constraints, Computers & Geosciences, 36, 441–452, 2010.

Durand-Riard, P., Salles, L., Ford, M., Caumon, G., and Pellerin, J.: Understanding the evolution of syn-depositional folds: Coupling decompaction and 3D sequential restoration, Marine and Petroleum Geology, 28, 1530–1539, 2011.

Durand-Riard, P., Guzofski, C., Caumon, G., and Titeux, M.-O.: Handling natural complexity in three-dimensional geomechanical restoration, with application to the recent evolution of the outer fold and thrust belt, deep-water Niger Delta, AAPG bulletin, 97, 87–102, 2013a.

Durand-Riard, P., Shaw, J. H., Plesch, A., and Lufadeju, G.: Enabling 3D geomechanical restoration of strike-and oblique-slip faults using geological constraints, with applications to the deep-water Niger Delta, Journal of Structural Geology, 48, 33–44, 2013b.

Fillon, C., Huismans, R. S., and van der Beek, P.: Syntectonic sedimentation effects on the growth of fold-and-thrust belts, Geology, 41, 83–86, https://doi.org/10.1130/G33531.1, 2013.

Fletcher, R. C. and Pollard, D. D.: Can we understand structural and tectonic processes and their products without appeal to a complete mechanics?, Journal of Structural Geology, 21, 1071–1088, 1999.

Fossen, H.: Structural geology, Cambridge University Press, 2016.

Fullsack, P.: An arbitrary Lagrangian-Eulerian formulation for creeping flows and its application in tectonic models, Geophysical Journal International, 120, 1–23, 1995.

Gassmöller, R., Heien, E., Puckett, E. G., and Bangerth, W.: Flexible and scalable particle-in-cell methods for massively parallel computations, arXiv preprint arXiv:1612.03369, 2016.

Gassmöller, R., Lokavarapu, H., Heien, E., Puckett, E. G., and Bangerth, W.: Flexible and Scalable Particle-in-Cell Methods With Adaptive Mesh Refinement for Geodynamic Computations, Geochemistry, Geophysics, Geosystems, 19, 3596–3604, https://doi.org/10.1029/2018GC007508, 2018.

Gassmöller, R., Lokavarapu, H., Bangerth, W., and Puckett, E. G.: Evaluating the accuracy of hybrid finite element/particle-in-cell methods for modelling incompressible Stokes flow, Geophysical Journal International, 219, 1915–1938, https://doi.org/10.1093/gji/ggz405, 2019.

Gerbault, M., Poliakov, A. N., and Daignieres, M.: Prediction of faulting from the theories of elasticity and plasticity: what are the limits?, Journal of Structural Geology, 20, 301–320, 1998.

Gerya, T.: Introduction to numerical geodynamic modelling, Cambridge University Press, 2019.

Glerum, A., Thieulot, C., Fraters, M., Blom, C., and Spakman, W.: Nonlinear viscoplasticity in ASPECT: benchmarking and applications to subduction, Solid Earth (SE), 9, 267–294, 2018.

Gratier, J.-P.: L'équilibrage des coupes géologiques. Buts, méthodes et applications., Géosciences-Rennes, 1988.

Groshong, R.: 3-D structural geology, Springer, 2006.

https://doi.org/10.5194/se-2020-89
Preprint. Discussion started: 27 May 2020

Guzofski, C. A., Mueller, J. P., Shaw, J. H., Muron, P., Medwedeff, D. A., Bilotti, F., and Rivero, C.: Insights into the mechanisms of fault-related folding provided by volumetric structural restorations using spatially varying mechanical constraints, AAPG bulletin, 93, 479–502, 2009.

Hassani, R., Jongmans, D., and Chéry, J.: Study of plate deformation and stress in subduction processes using two-dimensional numerical models, Journal of Geophysical Research: Solid Earth, 102, 17 951–17 965, 1997.

Heister, T., Dannberg, J., Gassmöller, R., and Bangerth, W.: High accuracy mantle convection simulation through modern numerical methods–II: realistic models and problems, Geophysical Journal International, 210, 833–851, https://doi.org/10.1093/gji/ggx195, 2017.

Hughes, T. J.: The finite element method: linear static and dynamic finite element analysis, Courier Corporation, 2012.

Hughes, T. J. and Taylor, R. L.: Unconditionally stable algorithms for quasi-static elasto/visco-plastic finite element analysis, Computers & Structures, 8, 169–173, 1978.

Ismail-Zadeh, A., Tsepelev, I., Talbot, C., and Korotkii, A.: Three-dimensional forward and backward modelling of diapirism: numerical approach and its applicability to the evolution of salt structures in the Pricaspian basin, Tectonophysics, 387, 81–103, 2004.

Jackson, M. P. and Hudec, M. R.: Salt tectonics: Principles and practice, Cambridge University Press, 2017.

Kaus, B. J., Mühlhaus, H., and May, D. A.: A stabilization algorithm for geodynamic numerical simulations with a free surface, Physics of the Earth and Planetary Interiors, 181, 12–20, 2010.

Koyi, H.: Salt flow by aggrading and prograding overburdens, Geological Society, London, Special Publications, 100, 243–258, 1996.

Kronbichler, M., Heister, T., and Bangerth, W.: High accuracy mantle convection simulation through modern numerical methods, Geophysical Journal International, 191, 12–29, 2012.

Louis-Napoléon, A., Gerbault, M., Bonometti, T., Thieulot, C., Martin, R., and Vanderhaeghe, O.: 3D numerical modeling of crustal polydiapirs with Volume-Of-Fluid methods, Geophysical Journal International, 2020.

Lovely, P., Flodin, E., Guzofski, C., Maerten, F., and Pollard, D. D.: Pitfalls among the promises of mechanics-based restoration: Addressing implications of unphysical boundary conditions, Journal of Structural Geology, 41, 47–63, 2012.

Maerten, F. and Maerten, L.: Unfolding and Restoring Complex Geological Structures Using Linear Elasticity Theory, in: AGU Fall Meeting Abstracts, 2001.

Maerten, L. and Maerten, F.: Chronologic modeling of faulted and fractured reservoirs using geomechanically based restoration: Technique and industry applications, AAPG bulletin, 90, 1201–1226, 2006.

Massimi, P., Quarteroni, A., and Scrofani, G.: An adaptive finite element method for modeling salt diapirism, Mathematical Models and Methods in Applied Sciences, 16, 587–614, 2006.

Massimi, P., Quarteroni, A., Saleri, F., and Scrofani, G.: Modeling of salt tectonics, Computer methods in applied mechanics and engineering, 197, 281–293, 2007.

Massot, J.: Implémentation de méthodes de restauration équilibrée 3D, Ph.D. thesis, Institut National Polytechnique de Lorraine, 2002.

Medwedeff, D. A., Jayr, S. N., and Lovely, P. J.: Practical and Efficient Three Dimensional Structural Restoration Using "Geological Knowledge-Oriented" Earth Models, in: AAPG Annual Convention and Exhibition, 2016.

Moresi, L., Dufour, F., and Mühlhaus, H.-B.: A Lagrangian integration point finite element method for large deformation modeling of viscoelastic geomaterials, Journal of Computational Physics, 184, 476–497, 2003.

Moretti, I.: Working in complex areas: New restoration workflow based on quality control, 2D and 3D restorations, Marine and Petroleum Geology, 25, 205–218, 2008.

https://doi.org/10.5194/se-2020-89
Preprint. Discussion started: 27 May 2020

Moretti, I., Lepage, F., and Guiton, M.: KINE3D: a new 3D restoration method based on a mixed approach linking geometry and geomechanics, Oil & Gas Science and Technology, 61, 277–289, 2006.

Morra, G. and Regenauer-Lieb, K.: A coupled solid–fluid method for modelling subduction, Philosophical magazine, 86, 3307–3323, 2006.

Muron, P.: Méthodes numériques 3-D de restauration des structures géologiques faillées, Ph.D. thesis, INPL, 2005.

Nalpas, T. and Brun, J.-P.: Salt flow and diapirism related to extension at crustal scale, Tectonophysics, 228, 349–362, 1993.

Parquer, M. N., Collon, P., and Caumon, G.: Reconstruction of Channelized Systems Through a Conditioned Reverse Migration Method, Mathematical Geosciences, 49, 965–994, 2017.

Pellerin, J., Lévy, B., Caumon, G., and Botella, A.: Automatic surface remeshing of 3D structural models at specified resolution: A method based on Voronoi diagrams, Computers & Geosciences, 62, 103–116, 2014.

Poliakov, A., Cundall, P., Podladchikov, Y., and Lyakhovsky, V.: An explicit inertial method for the simulation of viscoelastic flow: an evaluation of elastic effects on diapiric flow in two-and three-layers models, in: Flow and Creep in the Solar System: observations, modeling and Theory, pp. 175–195, Springer, 1993.

Poliakov, A. N., Podladchikov, Y. Y., Dawson, E. C., and Talbot, C. J.: Salt diapirism with simultaneous brittle faulting and viscous flow, Geological Society, London, Special Publications, 100, 291–302, 1996.

Quinquis, M. E., Buiter, S. J., and Ellis, S.: The role of boundary conditions in numerical models of subduction zone dynamics, Tectonophysics, 497, 57–70, 2011.

Ramberg, H.: Instability of layered systems in the field of gravity., Physics of the Earth and Planetary Interiors, 1, 427–447, 1968.

Ramberg, H.: Gravity, deformation and the earth's crust: in theory, experiments and geological application, Academic press, 1981.

Ramón, M. J., Pueyo, E. L., Caumon, G., and Briz, J. L.: Parametric unfolding of flexural folds using palaeomagnetic vectors, Geological Society, London, Special Publications, 425, 247–258, 2016.

Robey, J. M. and Puckett, E. G.: Implementation of a volume-of-fluid method in a finite element code with applications to thermochemical convection in a density stratified fluid in the earth's mantle, Computers & Fluids, 190, 217–253, 2019.

Rose, I., Buffett, B., and Heister, T.: Stability and accuracy of free surface time integration in viscous flows, Physics of the Earth and Planetary Interiors, 262, 90–100, 2017.

Rouby, D.: Restauration en carte des domaines faillés en extension. Méthode et applications., Ph.D. thesis, Université Rennes 1, 1994.

Royden, L. and Keen, C.: Rifting process and thermal evolution of the continental margin of eastern Canada determined from subsidence curves, Earth and Planetary Science Letters, 51, 343–361, 1980.

Schubert, G., Turcotte, D. L., and Olson, P.: Mantle convection in the Earth and planets, Cambridge University Press, 2001.

Tang, P., Wang, C., and Dai, X.: A majorized Newton-CG augmented Lagrangian-based finite element method for 3D restoration of geological models, Computers & Geosciences, 89, 200–206, 2016.

Thielmann, M., May, D., and Kaus, B.: Discretization errors in the hybrid finite element particle-in-cell method, Pure and Applied Geophysics, 171, 2165–2184, 2014.

Thieulot, C.: FANTOM: Two-and three-dimensional numerical modelling of creeping flows for the solution of geological problems, Physics of the Earth and Planetary Interiors, 188, 47–68, 2011.

Thieulot, C., Steer, P., and Huismans, R.: Three-dimensional numerical simulations of crustal systems undergoing orogeny and subjected to surface processes, Geochemistry, Geophysics, Geosystems, 15, 4936–4957, 2014.

Thieulot, C. C.: Fieldstone: The Finite Element Method in Computational Geodynamics, https://doi.org/10.23644/uu.9209393.v1, https://uu.figshare.com/articles/manual_pdf/9209393, 2019.

https://doi.org/10.5194/se-2020-89
Preprint. Discussion started: 27 May 2020

Trim, S., Lowman, J., and Butler, S.: Improving mass conservation with the tracer ratio method: application to thermochemical mantle flows, Geochemistry, Geophysics, Geosystems, 2019.

van Keken, P., King, S., Schmeling, H., Christensen, U., Neumeister, D., and Doin, M.-P.: A comparison of methods for the modeling of thermochemical convection, Journal of Geophysical Research: Solid Earth, 102, 22 477–22 495, 1997.

Willett, S., Beaumont, C., and Fullsack, P.: Mechanical model for the tectonics of doubly vergent compressional orogens, Geology, 21, 371–374, 1993.

Zehner, B., Hellwig, O., Linke, M., Görz, I., and Buske, S.: Rasterizing geological models for parallel finite difference simulation using seismic simulation as an example, Computers & geosciences, 86, 83–91, 2016.